-

MASTER THESIS

Development of a Cryocooler-based Remote Cooling System at Low Temperature

Author :
Mr. Boyan NAYDENOV

Supervisors :
Dr. Torsten KOETTIG
Dr. Nicolas GOURDAIN

Advisor :
Ms. Aleksandra ONUFRENA

November 6, 2020

Acknowledgements

I would like to offer my special thanks to Dr. Torsten Koettig, my supervisor at CERN, for his patient guidance and for sharing his profound expertise and great enthusiasm on the research subject. I would also like to express my very deepest appreciation to Aleksandra Onufrena, for her invaluable explanations and advices, and for the exceptional energy she puts into our everyday work.

I would like to thank my university supervisor, Prof. Nicolas Gourdain, for the received support, and all the administrative department staff, who guided my internship relentlessly, even during the hardest conditions set by a pandemic.

Finally, I am very grateful to the entire Cryolab team for creating such a great working atmosphere.

Contents

List of acronyms

AC	*Alternate Current*
CCC	*Cryogenic Current Comparator*
CIF	*Cooling Interface*
CMS	*Compact Muon Solenoid*
CP	*Critical Point*
CFHEX	*Counter-Flow Heat Exchanger*
DC	*Direct Current*
EOS	*Equation of State*
FVM	*Finite Volume Method*
GM	*Gifford-McMahon*
HEX	*Heat Exchanger*
HP	*High Pressure*
HTS	*High Thermal Superconductor*
IF	*Interface*
JT	*Joule-Thomson*
LHC	*Large Hadron Collider*
LP	*Low Pressure*
MLI	*Multi-Layer Insulation*
MRI	*Magnetic Resonance Imaging*
NBP	*Normal Boiling Point*
PID	*Proportional–Integral–Derivative*
PT	*Pulse Tube*
RF	*Radio Frequency*
RTD	*Resistance Temperature Detector*
SC	*Superconductor*
SQUID	*Superconducting QUantum Interface Device*
TP	*Triple Point*

Introduction

The field of cryogenics is focused on conducting technology and material development as well as generic research at low temperatures, namely below -150 °C. One of the advantages of working at these temperatures is related to the changes in material properties. For example, the resistance of electrically conducting materials decreases at lower temperatures, allowing more current to be conducted. For a certain type of materials, the direct current resistance is fully eliminated (see more in Sec. 1.2.1), which enables a wide range of applications.

The cooling to low temperatures can be enabled in a number of ways and is often provided using liquefied gases. When large heat loads, e.g. > 3 kW at 40 K, need to be evacuated at low temperatures, cryogenic plants can present a solution. For lower power (< 200 W at 40 K) applications, the cryocoolers (described in more detail in Sec. 1.2) can be used. For intermediate cooling powers (200 W - 3 kW) range, a general solution has not yet been established [11]. Remote cooling systems that are currently under development in the Cryolab aim to cover this gap in the cooling needs for a range of applications, e.g. medical, physics, etc. (see Sec. 2.2).

CERN is one of the top research institutions in the world when it comes to cryogenics. It has a very strong expertise in cooling large superconducting magnets down to 1.9 K. Currently, it is enlarging its know-how through R&D into remote cooling options, as this technology has a potential to have significant economical advantages compared to the traditional liquid-bath cooling.

It is in this context that this thesis has been carried out. Aleksandra Onufrena, a PhD student at the CERN Cryogenic Laboratory, is focusing her research on a compact and highly effective heat exchanger design. This is a fundamental part of the remote cooling systems under development, since its effectiveness determines the performance of the entire system in terms of the total cooling power that it can generate.

The project I am undertaking in this master thesis is focused on the characterisation of the designed and manufactured heat exchanger through experimental measurements as well as through simulation analysis. Moreover, different system architectures for remote cooling systems are analysed and simulated. The main objective of this activity is to analyse the viability of such systems for different applications, mainly at CERN. In additon, a numerical tool aiming to facilitate the extraction of fluid properties for thermodynamic simulations is developed.

The report has been structured in four parts. Chapter 1 gives the background information about cryogenics and CERN, necessary to follow the following chapters. Chapter 2 introduces the remote cooling systems concept and their main applications. The performed system studies are also presented, together with the relevant results. Chapter 3 is focusing on the heat exchanger characterisation. It describes the different measurement campaigns that were performed and the analysis of the obtained results. Chapter 4 presents the developed tool for thermophysical properties querying.

Chapter 1

Context: CERN, Cryogenics and Cryolab

1.1 CERN

The state of the European scientific community after the Second World War was substantially damaged. To address this, in 1949, the french physicist Louis de Broglie, made the first official proposal for the creation of a European Laboratory. Two years later, a resolution for the establishment of the European Council for Nuclear Research was approved with a clear objective of fostering international collaboration and bringing together European scientists. The CERN acronym came from the name in French, where it was called *Conseil Européen pour la Recherche Nucléaire*. Later on, the organism expanded its area of research from the nucleus to the broader particle physics. From that point on, the laboratory is referred as the European Laboratory for Particle Physics, but the acronym was kept as its name. Geneva was selected for locating the organisation. Its central European location, the Swiss neutrality during the World Wars and the number of international organisations existing in the area, played a key role in the decision.

CERN's first accelerator, the 600 MeV Synchrocyclotron, was built already in 1957, focusing on pure nuclear physics for the following 33 years. The Proton Synchrotron (PS), started operating in 1959, initiating the CERN's particle physics programme. New accelerators and plenty of experiments have been built since then. Some of the most relevant landmarks in the history [13] of the organisation are summarised below:

- In 1968, during the revolution of transistor amplifiers, Georges Charpak developed the "multiwire proportional chamber", a gas-filled box with many parallel detector wires, each connected to individual amplifiers. This chamber changed particle detection forever, going from manual photographs examinations to electronic computer analysis with a counting rate a thousand times better than existing techniques at the time. Charpak was awarder the Physics Nobel prize for his invention. Today, the set of experiments at CERN generate about 50 petabytes of data per year, using techniques based on the multiwire proportional chamber.

- In 1971, the PS would create the world's first interactions from colliding protons.
- The same year, the construction of the seven kilometre circumference Super Proton Synchrotron (SPS) was approved. It still runs today, reaching energies up to 450 GeV.
- In 1983, CERN announces the discovery of the W and Z bosons, carriers of the weak interaction between particles, thanks to the proton-antiproton collisions produced at the SPS.
- In July 1989, the Large Electron-Positron (LEP) collider was commissioned. It was the largest electron-positron accelerator ever built, with an impressive 27 km circumference. It is the predecessor of the Large Hadron Collider (LHC).
- The same year, Tim Barners-Lee invents the World Wide Web while working at CERN. The first website ever can be consulted at `http://info.cern.ch/`. Four years later, CERN made a public release available with an open licence, allowing the web to become what it is today.
- In 1995, antiatoms were produced at CERN for the first time. More specifically, antihydrogen.
- In 2006, ATLAS Barrel Toroid, the world's largest superconducting magnet ever built was switched on, storing an energy of 1.1 GJ.
- In 2008, the LHC is finally ready and switched on. Its 8 years design and assembly implied an immense progress in areas such as superconductivity, magnets, electronics, cryogenics, computers, etc. Eventually, the LHC would reach energies up to 13 TeV of total energy per collision.
- In 2012, the long sought Higgs Boson is observed in the LHC by the ATLAS and the CMS experiments. It represents the visible manifestation of the Higgs field, which is responsible for giving mass to particles.

Currently, CERN is in its Long Shutdown[1] 2 performing major maintenance and preparation for the future High-Luminosity (HiLumi) LHC upgrades, which is planned to be fully implemented during the Long Shutdown 3, between 2025 and 2027[2]. Once the HiLumi

[1] The accelerators chain is not running during the shutdown.
[2] `https://home.cern/news`

implementation is ready, the LHC should be able to generate more collisions. Ten times more data is expected, maximising the chances to detect extremely rare phenomena. To acquire and post-process that amount of data, detectors require ambitious upgrades which will be carried out during the next years.

In the long term, CERN's focus is on its Future Circular Collider (FCC) proposal. Its main aim is to reach collision energies of 100 TeV, which is about 8 times the current levels. It is still in the preliminary phase, examining three different types of particle collisions: hadron-hadron collisions like in the LHC, electron-positron collisions as in the former LEP, and proton-electron collisions.

(a)

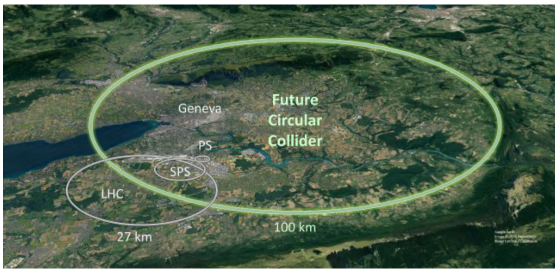

(b)

Figure 1.1: CERN accelerator complex; (a) photo of the LHC tunnel with an array of the superconducting magnets (blue); (b) bird's-eye view on the location of the CERN accelerator complex including the PS, SPS and LHC rings. The foreseen location of the 100 km-long Future Circular Collider (FCC) is also indicated [13].

Developing, operating and maintaining all the facilities and experiments at CERN requires a great expertise in many highly technical areas such as radio-frequency, vacuum, cryogenics, magnets, superconductivity, etc. Among those, cryogenics stands out as an ubiquitous field that is necessary for the operation of numerous facilities on site.

1.2 Cryogenics

Cryogenics is defined by the Cambridge Dictionary as "The scientific study of very low temperatures and how to produce them." In general, the term has been used to refer to temperatures below $-150\,°C$.

At CERN, the LHC has the largest cryogenic system in the world, which is one of the coldest places on earth. This cryogenic plant is used to cool down the NiTi wire coils that form up the superconducting electromagnets that are used inside the LHC to steer and focus the particle beams. As the magnets are in their superconducting state, their electrical resistance is practically removed, thus very large currents (up to 13 kA) can be conducted, resulting in an extremely high 8.3 T magnetic field. The cryogenic system ensures that the magnets operate at their necessary temperature, that is, at 1.9 K[3]. 120 t of helium is used as a liquid coolant because helium remains in its liquid state at these temperature levels.

The cooling process is divided in three stages. First, two cryo-plants cool down helium gas to 80 K with the help of liquid nitrogen. Next, helium is brought to 4.5 K via a series of pre-cooling heat exchangers (HEX) and expansion turbines. Lastly, helium's pressure is reduced down to 15 mbar in order to reach the required 1.9 K in saturation conditions. A particularity about helium is that it presents a phase transition point at 2.17 K, the so called lambda point (see Sec. 1.2.3), under which it becomes a superfluid. In that state, it has a very high thermal conductivity and very low viscosity. This makes it ideal for cooling since it can creep into small gaps in the superconducting magnet structure and carry away the heat efficiently. Such temperature changes necessarily imply a significant contraction of the materials. In total, the entire magnet chain of the LHC contracts by 80 m when it is cooled down. This presents a great challenge that is normally addressed with special flexible interconnections between the magnets.

1.2.1 Superconductivity

Even though the biggest cryogenic application at CERN is the LHC, there are plenty of other facilities where very low temperatures are needed. The experiments located along the LHC have very low temperature requirements, with the Compact Muon Solenoid (CMS) having its own cryogenic plant.

What most of these systems have in common is superconductivity, a research field that goes in hand with cryogenics. In short, electrical resistance of electrical conductors reduces drastically with temperature. For special types of materials, namely superconductors (SC), below a certain critical temperature, usually <30 K, the DC resistance disappears completely and the AC impedance is reduced drastically. There is a high interest in using these for a number of applications, and cryogenics is needed to ensure their operation. Once the temperature raises above the superconductor critical temperature T_{cr}, it loses its superconducting state. Exceptions are, e.g., the ceramic high temperature SC[4].

[3] For reference, the temperature of outer space is 2.7 K

[4] A lot of research is currently being done on high-temperature superconductors (HTS), i.e., those that can be maintained in a superconducting state with liquid nitrogen (77 K).

The LHC electromagnets mentioned before are one example where superconductivity and cryogenics are applied at CERN. The superconducting state allows a magnet to generate a higher magnetic field due to its much higher operating DC current. In turn, this reduces the total length of the LHC tunnel and the total amount of heat load that needs to be removed, considerably. Superconducting QUantum Interface Devices (SQUIDs) are another relevant example. They consist in a very high-sensitivity magnetometer sensor that is used at some detectors at CERN and also for a broad range of other applications (eg.: Magnetic Resonance Imaging (MRI), oil prospecting, earthquake prediction, gravitational waves detection, etc.). It needs to be kept at low temperatures in order to keep its superconducting state.

Radio Frequency (RF) cavities can also operate in a superconducting state. Their function is to accelerate charged particles in a particle accelerator so that they reach the desired collision energy. Basically, it consists of a container crossed by the beam in which a specific RF frequency resonates, creating an accelerating electric field for the passing particles. Those are synchronised with the cavity frequency so that the voltage is used to accelerate them, increasing their energy in turn.

1.2.2 Non-CERN related applications

Outside of CERN, cryogenics is a field in expansion in many different industries and thrilling applications [14]. A small review of those follows:

- **Cryogenic electronics**: Both semi-conducting and superconducting devices can benefit from operating at low temperatures. Lower noise, better quality factor, improved thermal and electrical conductivity, losses reduction or increased speed are some examples of the potential gains from low temperature electronics.
- **Cryogenic treatment of materials**: Consists in slowly cooling down a material and keeping it at this temperature temporarily, followed by a gradual increase to room temperature. This has shown to provoke an increased wear resistance and hardness. Such a processing is commonly used on industrial tooling in order to increase the life duration of industrial tools.
- **Medical applications**: Cryogenics is used for cryosurgery, to freeze and destroy undesirable tissues and for cancer treatment. The latter is done with the aid of particle accelerators that use superconducting magnets.
- **Space**: Space industry has profited significantly from cryogenic advances in the last years. Many science missions use detectors that operate at low temperatures. For example, space telescopes are benefiting from cryogenics since operating at such low temperatures reduces the telescope thermal emissions and noise, en-

hancing its sensitivity, significantly. Preservation of biological samples and material gathered from comets or other planets is another area that uses cryogenic technology. Lastly, liquid propulsion has been using cryogenic propellants such as liquid hydrogen and liquid oxygen because of their high specific impulse. Traditionally, those have been stored in poorly insulated tanks since the propellants are mostly consumed during the launch. For long duration missions this can be a problem because of propellant leaks and losses, hence, there is an interest in extending its storage time.

- **Aeronautics**: Testing in cryogenic wind tunnels can be performed over a larger range of Reynolds numbers compared to the non-cryogenic ones, allowing them to better recreate aircraft operational conditions. Also, Airbus, one of the biggest aircraft manufacturers, is currently heading into the direction of hydrogen powered aircraft [19] with the purpose of creating a zero-emission commercial airplane. Due to the extremely low energy density of hydrogen in the gas phase at ambient pressure and temperature, it has to be kept at either a very high pressure or in liquid state. The latter requires cryogenic cooling. Also, if superconductivity is deemed beneficial for the concept, a distributed cryogenic cooling would be necessary. All in all, the future of cryogenics in aeronautics is certainly promising.

The following sections of this chapter will give an introduction on some relevant cryogenic concepts. Different cryogenic coolants (cryogens) will be presented along with the different possibilities to reach such low temperatures.

1.2.3 Cryogens

Any fluid that operates below 150 K is considered to be a cryogen. It can also be referred to simply as cryogenic fluids. The most common cryo fluids and their properties are presented in Tab. 1.1. First, let us review some important concepts about the different phases of a fluid.

A phase diagram illustrates the state of the material at a given temperature and pressure. A generic example of such a diagram is presented in Fig.1.2. There are two important points which define the general behaviour of the fluid:

- **Triple point (TP)**: the point at which liquid, vapour and solid coexist.
- **Critical point (CP)**: the point from which the liquid and gaseous state of the substance are not distinguishable. Above this point, only one phase exists, which is both liquid and gas, namely supercritical fluid.

An auxiliary point has been defined for the sake of the explanation, called **Normal Boiling Point (NBP)**, defining the temperature at which the gas condenses, or the liquid evaporates, for a sea-level pressure (1 bar). The NBP is useful to explore the state of the fluid at ambient-pressure condition.

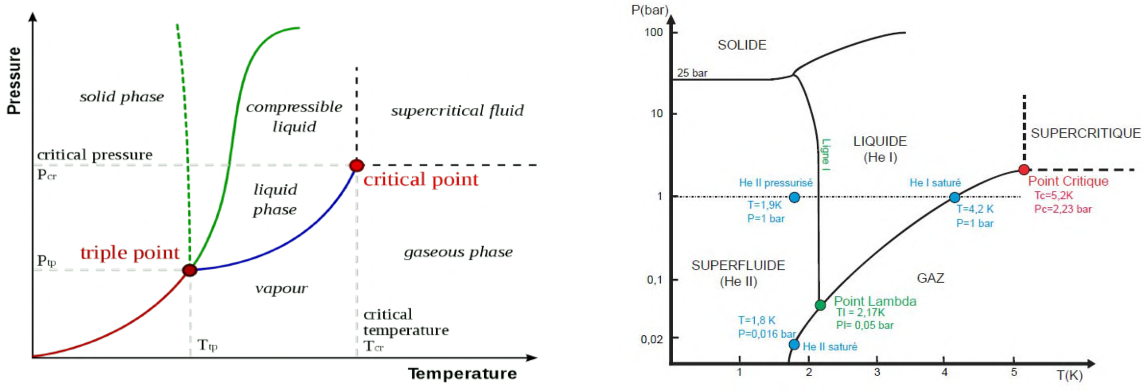

(a) (b)

Figure 1.2: Phase diagrams presenting the variation of the state of the fluid at different temperature and pressure conditions; (a) generic example with the critical and triple points marked and (b) helium phase diagram where, in addition to the critical point, the lambda point and line are shown indicating the location of He I to He II phase transition [13].

The NBP, the TP and some examples of applications are presented in Tab. 1.1 for the most common cryogenic fluids in descending NBP order. Several relevant conclusions can be drawn from these properties.

Some gases like methane and hydrogen are highly-flammable. Oxygen presents a slightly magnetic and a strong reactive behaviour. Availability of the fluid is a characteristic that will strongly influence the price. Nitrogen is abundant nowadays as it is produced in large quantities for air liquefaction plants, hence, is relatively cheap. Lastly, and probably most importantly for cooling applications, the NBP gives an idea of the levels at which the cryogen can be used for refrigeration near room pressures. Only helium has the capacity to remain liquid at the temperatures needed for the CERN applications described above. It reaches 4.2 K at 1 bar, which offers a lot of possibilities.

NBP temperature of helium is already interesting for many superconducting materials which have their critical temperature above it. LHC magnets are made of a Niobium-Titanium (NbTi) alloy which has a critical temperature of 10 K. Therefore, helium is used as a refrigerant for the SC magnets offering the advantages of being inert, which simplifies safety concerns considerably.

A unique property of helium is that it does not have a triple point. Thus, it never solidifies below ~25 bar. Instead, it has a lambda point and a lambda line shown in Fig. 1.2b. The former is defined at 2.17 K and 0.050 bar and separates two different states of helium. Normal helium (He I) to the right, with superfluid helium (He II) to the left. Both are liquid, but the latter presents a completely different set of properties. Notably, it has very low viscosity and very high thermal conductivity. Those two properties make it a perfect refrigerant as it fills the small gaps within structures while absorbing the heat very efficiently.

Since helium offers the best suitability for CERN's applications, it will be the main referred cryogen for the rest of the report.

Cryogen	**Boiling point at** 1 bar **(NBP)**	**Triple Point (TP)**	**Uses**	**Properties**
Methane	117.7 K	88.7 K, 1010 mbar	Fuel	Inflammable.
Oxygen	90.2 K	54.4 K, 1.5 mbar	Rocket Fuel and medical gas storage.	Magnetic and reactive (enhances burning)
Argon	87.3 K	68.6 K, 680 mbar	Inert atmosphere during material processing.	Non-magnetic and inert.
Nitrogen	77.3 K	63 K, 125 mbar	Cryogenic conditioning and HTS cooling.	Non-magnetic, inert and cheap.
Neon	27.1 K	24.6 K, 430 mbar	Intermediate temperature refrigerant.	Non-magnetic, inert and rare.
Hydrogen	20.3 K	13.8 K, 700 mbar	Rocket fuel, materials processing and fusion reactors.	Inflammable.
Helium	4.2 K	no TP, $T_\lambda = 2.178$ K	Low temperature coolant and superconductivity.	Inert and superfluid phase.

Table 1.1: Typical cryogens properties[6] demonstrating the ability of liquid helium as low-temperature coolant.

1.2.4 Cryogenic cooling systems

The two main ways to provide cryogenic cooling for a long and sustained operation are bath cryostats run by a **cryoplant**, and **cryocoolers**.

A cryoplant targets very high heat loads applications. Its high implementation and operation cost is not justified for loads under 1 kW at 40 K or 0.1 kW at 4 K. The cryoplants cooling the LHC are based in this principle and, as previously seen, they reach up to 18 kW at 4.5 K.

A cryocooler, on the other hand, has a low cooling power capacity. Currently, the best models on the market can reach 100 W at 40 K or 2 W at 4.2 K [11].

Both methods use a cryostat to support its operation. A cryoplant circulates cryogenic liquid in a cryostat that contains the cooling interface (CIF), ensuring that the cooled device is always submerged in a bath by evacuating the boiled cryogen and by refilling it continuously. Conversely, a cryocooler needs to be located inside a cryostat, insulated from exterior heat loads in order to fully administrate its cooling power to the CIF.

Cryostats

Cryostats or dewars are bigger and more sophisticated versions of a thermos bottle. They consist of a volume designed to keep fluids or other devices at very low temperatures, insulating its content as well as possible from external heat loads. Normally, a cryostat is a combination of two outer layers providing vacuum and thermal radiation insulation. The cooled device and much of the necessary support equipment are placed inside.

Cryocoolers

A cryocooler is a machine that operates inside a dry cryostat, i.e. there is no need for a liquid bath since now the cryocooler is the cold source. This is an active device creating the cooling by itself. There is a range of cryocoolers based in different cooling cycles. The most common ones are the Pulse Tube (PT) and the Gifford-McMahon (GM) cryocoolers.

A GM cryocooler is an alternating machine that consists of a compressor, a regenerator (that can be made out of a woven metal mesh) and a displacer. It operates based on the Stirling cycle. In short, it compresses the working fluid, which is typically helium, then the displacer moves together with the compressed helium along the cold regenerator, which cools the helium down. Next, helium is expanded creating the useful cooling power at the interface where the heat load can be dissipated. Finally, the displacer moves back to its initial position together with the cold helium, which cools down the regenerator, preparing it for the next cycle. The process is repeated continuously providing a constant cooling at the end of the cryocooler coldhead.

The displacer of the GM cryocooler is a moving part that can create reliability issues, and vibrations, which could be transmitted to the cooled device. In a PT crycooler the displacer is replaced with a virtual gas piston, making the cryocooler more reliable and less prone to vibrations.

(a)

(b)

Figure 1.3: Pictures of Sumitomo cryocoolers [17]; (a) 2-stage GM cryocooler with a mechanical displacer (RDK-101D 4K) and (b) 2-stage PT cryocooler with a gas displacer, in U-shape coldhead design. (RP-082B2 4K PT).

1.3 Cryolab

The thesis is carried out within the CERN's Central Cryogenics Laboratory (Cryolab), which is part of the Cryolab and Instrumentation Section of the Cryogenics Group of the Technology Department. It is a multipurpose cryogenic laboratory equipped to support both internal CERN and external clients. Several activities take place within the laboratory:

- Cryogenic design, instrumentation and safety consultancy,
- Providing test facilities,
- R&D,
- Design, build-up and commissioning of cryogenic systems,
- Design, build-up, commissioning, operation, measurement and data analysis of a cryogenic system,
- Training and outreach.

Chapter 2

Remote Cooling System

The two existing ways of cooling a device down to very low temperatures were introduced in Sec.1.2.4. A cryoplant based liquid cryogen bath cooling, and a cryocooler, also referred to as cryogen-free cooling.

The main advantages of the presented boiling liquid cryogen bath system supported by a cryoplant, is its elevated and stable cooling power as well as its low vibrations on the CIF. Its main problem is the eventual warm up and boil off of the cryogen, which leads to an increase in pressure. To maintain the pressure within the safe limits, the system needs to be monitored and equipped with safety valves and an exhaust system. Keeping the device constantly submerged requires the cryogen to be periodically refilled. Such conditions create high maintenance requirements. This may not be a problem in a laboratory environment but, for long term operations, such a solution might be impractical and expensive as large amount of cryogen would be required. Furthermore, if applied to measurement devices, most probably the cryostat will have an opening, as in the RF cavity from Fig. 2.1a, to the outside in order to measure its target variable. Having an opening in a bath cryostat is a big thermal challenge.

In contrast, the cryogen-free cooling systems (see Fig. 1.3) are typically smaller in size and weight, and eliminate the difficulties related with the purchase and use of cryogenic liquids. Safety issues related with cryogen boil-off are also reduced. These represent some important advantages, especially for an autonomous independent system such as an MRI scanner. Nevertheless, new challenges appear with such designs. The cryocooler typically offers less cooling power which limits its use to applications where the heat loads that need to be evacuated at low temperature are small. Also, since it is based on an active alternating machine, it generates vibrations which can be transmitted to the cooled device. Lastly, the connection from the cryocooler cold stage to the heat load can be challenging to implement for certain applications.

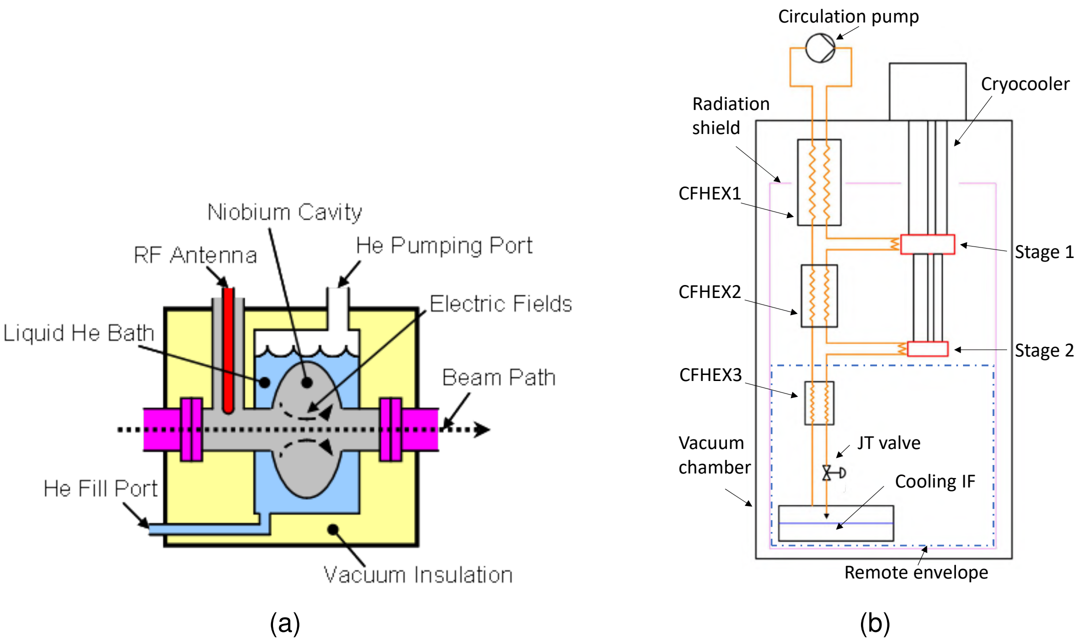

Figure 2.1: Schematic of cooling options; (a) cooling is provided to the RF cavity to keep it in superconducting state. It is submerged in a liquid-helium bath inside a cryostat. The pumping port ensures that the boiled helium is evacuated while the fill port keeps filling liquid helium in order to keep the cavity submerged. The beam is accelerated while crossing the cavity; (b) cryocooler based system with an independent convection loop where the fluid is circulated by the pump at the top. The fluid is pre-cooled in the three CFHEX and delivered to the CIF, located in a remote envelope. The JT-valve expansion increases the cryocooler cooling power.

While both options present some advantages and drawbacks, their main difference is in their application scale. The liquid cryostat option is very suitable for large scale applications that require high cooling powers and that can afford having a cryoplant nearby, producing all the necessary cryogen. Cryocoolers, on the other hand, target turnkey, stand-alone and compact use cases where cooling power requirements are lower. A gap for intermediate cooling power levels exists between those two systems. The focus of remote cooling research is to close this gap by enhancing the stand-alone cryogen-free approach, having the potential to distribute the localised cooling at remote locations, while also increasing the available cooling powers.

The main purpose of a remote cooling system is to physically decouple the cryocooler from the cooled device. Such decoupling (see Fig. 2.1b) would give the following advantages:

- Cryocooler vibrations are not transmitted to the cooled device, which is crucial for high-sensitivity sensors.

- Gained distance between the cold source and the cooled device benefits cases where the latter operates in a harsh environment that can damange or worsen the cryocooler performance. A good example is a radiation test environment.
- Innovative designs can be included in the transfer line in order to increase the cooling power.

This approach can be accomplished by flexible copper or aluminium straps or with a cryogen convective pipe, both connecting the cryocooler cold head with the heat load. The first option has severe limitations in terms of power since it relies only on conduction. If high heat loads have to be dissipated, such straps would have to be very bulky. This option is only valid for temperatures above 20 K [4]. A transfer convective pipe on the other hand, has a greater cooling capacity since it uses an already moving mass to transport the cooling power. Therefore, convection is added to the conduction enhancing its cooling power at the CIF. Moreover, such an option offers more resilience against mechanical and thermal oscillations coming from the cryocooler. Fig. 2.1b presents a circulation loop that uses such a convective pipe. Different configurations of the circulation circuit create specific performances. Therefore, several circulation systems were simulated in order to decide on their fitness for different applications. The next section presents the followed procedure and the obtained results.

2.1 The concept

Special care has to be taken in transferring the limited available cooling power at the cryocooler, to the heat load. Certain designs may increase this power significantly. When working on the design of the system, the goal is to achieve maximum cooling power at the lowest possible temperatures without transferring the vibrations to the cooled device.

The remote cooling system under development consists of one cryocooler and an independent convection loop or circulation system. The latter is based on the Linde-Hampson refrigeration cycle [1]. Its purpose is to transport the cooling power provided by the cryocooler to the CIF of the cooled device in the most effective way. Pre-cooling heat exchangers are critical components for the overall performance. Choosing the operation conditions is not straightforward. The mass flow rate needs to match the cooling power of the cryocooler interfaces. Also, the inlet pressure of the convection loop has to be selected carefully so that maximum expansion is achieved with the JT-valve.

Fig. 2.1b shows a cryocooler-based cooling system with a convection loop. The latter is composed of:

- A pump, which will ensure the continuous circulation of the fluid.
- Three counter-flow heat-exchangers (CFHEX) where the high-pressure flow is pre-cooled by a colder returning low-pressure flow.
- Two heat exchangers at each of the cryocooler's stages to pre-cool the HP fluid flow.
- A JT-valve, where the flow expands from high to low pressure. Such an expansion can produce a cooling effect if it happens below the inversion curve of the fluid.

The outlet pressure for the designated system is 1 bar at the inlet of the vacuum pump, to avoid under-pressure with regard to ambient conditions[1]. As a consequence, the outlet pressure combined with the pressure drop of the three counter-flow heat exchangers determines the pressure downstream the JT-valve. This can be seen clearly in the helium p-h diagram in Fig. 2.2, where the two-phase area is entered by the JT-expansion. The larger the created pressure drop by the JT-expansion is, the lower the final temperature at the CIF is. Also, the lower the staring enthalpy of the JT-expansion is, the bigger the cooling power will be (see Fig. 3.1). However, the curved shape of the isotherms represents a limit for the pressure. Increasing the inlet pressure further than its peak would actually reduce the amount of liquid helium produced in the expansion since the isotherm turns to the higher enthalpies. This, in turn, leads to less cooling power being produced.

From Fig. 2.2 one can also see that when expanding from 5 K isotherm, the HP pressure to generate the largest amount of liquid would lie around 3 bar. However, the amount of liquid produced does not increase significantly if the expansion is started at a lower, e.g. 2.5 bar pressure. Thus, working at this pressure may be a more favourable choice as less effort is required to pressurise the fluid at the inlet of the system.

The state of the fluid at the CIF, i.e., where the useful cooling will be extracted, is what will define the characteristics of the cooling. For the example in Fig. 2.2, a two-phase flow was considered. This is beneficial as it provides a constant temperature across the CIF, which is typically preferred compared to having a temperature gradient. However, the two-phase flow can induce some vibrations into the CIF due to the potential flow instabilities. To reduce the vibrations, an option could be to skip the JT-expansion and directly use the high-pressure fluid to provide cooling at the CIF. In this case, the flow velocity would be lower, hence less vibration would be transmitted to the cooled device. The operation at higher pressures also offers a possibility to use smaller pipelines and hence reduce the size of the transfer line system. However, no additional cooling power

[1]Operating in under-pressure conditions makes the system more complex as in-leaks from the outside have to be managed. Because of this, the system outlet pressure has been set to 1 bar.

would be produced without the expansion. When single-phase flow is required for a specific application, the best is to operate in the supercritical region of the cryogen, where it can not turn into a two-phase flow. However, for the case of helium, that region is found at higher than the operating temperatures. Therefore, a superliquid state is normally used for helium, that is, at $p > p_{sc}$ but $T < T_{sc}$. Depending on the desired system performance, the JT-valve can be located in one point or another. If two-phase flow is required it will naturally be before the CIF. If not, it can also be located in the return convection loop, at an appropriate temperature and pressure levels.

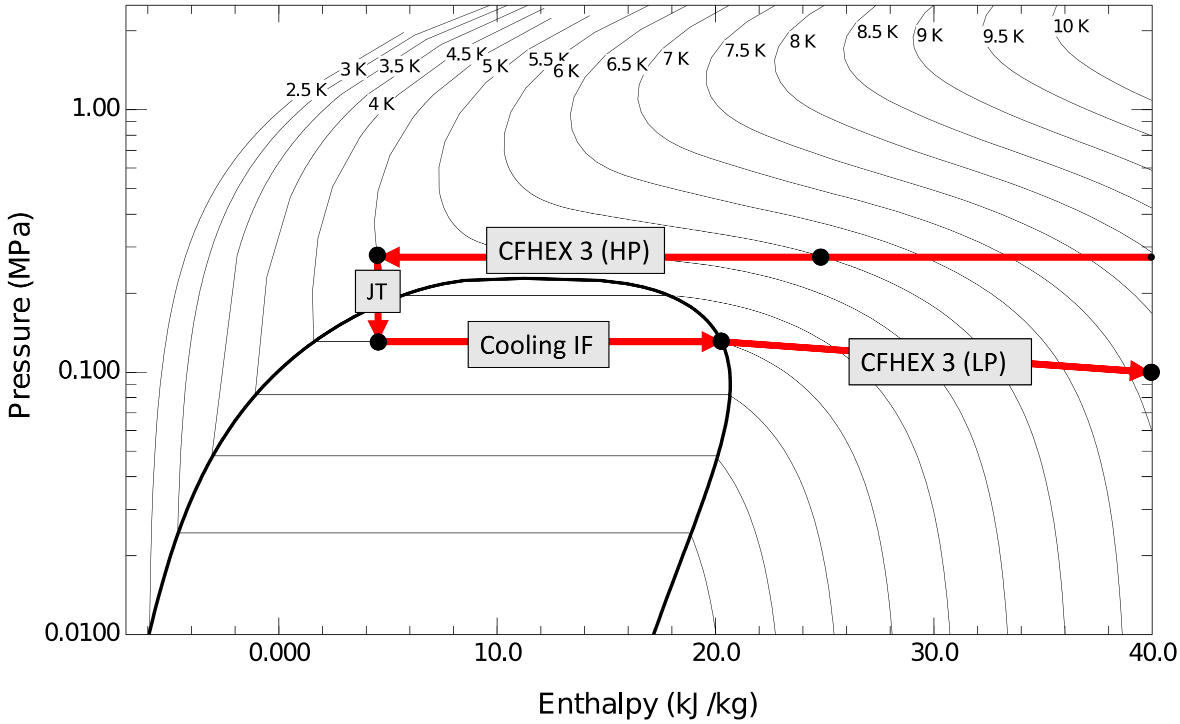

Figure 2.2: Pressure-enthalpy diagram of helium with the lower part of an example cooling cycle (in red) using a 4 K cryocooler as a cooling source. CFHEX3 is the third CFHEX presented in Fig.2.1b. Source: REFPROP.

The Joule-Thomson effect

The Joule-Thomson (JT) expansion, also known as a throttling process, is at use frequently in remote cooling systems. It is thus worth to briefly describe the effect on which it is based on. JT effect is a real gas effect that occurs when a gas passes through a narrow opening valve that is kept well insulated. This produces an isenthalpic expansion and a change of temperature. At room temperature, most gases would cool down upon expansion. Helium, hydrogen and neon, on the other hand, would warm up and would only cool down if below the inversion temperature T_{inv}. At one bar, helium has a T_{inv} of 45 K. Only below that temperature, the throttling would cool down the helium gas. The inversion temperature varies with pressure, so each case has to be checked.

The JT-coefficient μ_{JT} indicates whether the gas at a given temperature T, and pressure p is in a cooling region (positive) or in a warming region (negative). It is defined as follows:

$$\mu_{JT} = \left(\frac{\partial T}{\partial p}\right)_h \tag{2.1}$$

Where h is the enthalpy, which is constant during the expansion.

Since the ideal gas model assumes that both internal energy and enthalpy only depend on temperature, the JT-effect only exists for real gasses. The next lines demonstrate this statement.

Firstly, the enthalpy change dh, needs to be related with the entropy change dS. For that, the first principle of thermodynamics relating internal energy variation du, with heat supplied to the system dq and work done by the system $-dW$,

$$du = dq - dW \tag{2.2}$$

and the second one, relating the heat with the entropy variation ds,

$$dq = Tds \tag{2.3}$$

are combined into,

$$du = Tds - pdv \tag{2.4}$$

since the work done by the system is equal to pdv, where v is the specific volume. Now, remembering the definition of enthalpy:

$$h = u + pv \rightarrow dh = du + vdp + pdv \tag{2.5}$$

Combining eq.(2.4) and eq.(2.5) yields:

$$dh = Tds + vdp \tag{2.6}$$

Combining now, eq. (2.6) with the second Tds equation [8],

$$Tds = c_p dT - \mathrm{T}\left(\frac{\partial v}{\partial T}\right)_p dp \tag{2.7}$$

where c_p is the specific heat capacity at constant pressure, the following relation is obtained:

$$dh = c_p dT - \left[\mathrm{T} \left(\frac{\partial v}{\partial T} \right)_p - v \right] dp \tag{2.8}$$

Since the JT-valve gives an isenthalpic expansion, $dh = 0$. Combining eq. (2.1) with eq. (2.8) yields:

$$\mu_{JT} = \left(\frac{\partial T}{\partial p} \right)_h = \frac{1}{c_p} \left[T \left(\frac{\partial v}{\partial T} \right)_p - v \right] \tag{2.9}$$

Now, applying the derivative to the ideal gas law $pv = rT$, where r is the specific gas constant:

$$\left(\frac{\partial v}{\partial T} \right)_p = \frac{r}{p} = \frac{v}{T} \tag{2.10}$$

Substituting eq. (2.10) into eq. (2.9) gives:

$$\mu_{JT} = \frac{1}{c_p} \left[T \frac{v}{T} - v \right] = 0 \tag{2.11}$$

Eq. (2.11) proves that, for an ideal gas, $\mu_{JT} = 0$. Hence, an isenthalpic expansion does not provoke any temperature change unless a real gas is considered where internal energy and enthalpy depend on both temperature and pressure.

2.2 Remote cooling applications

Cryogenic refrigeration is most commonly implemented in the form of cooling inside a liquid cryogen bath. This approach is not ideal for some applications, as described in the introduction of the chapter. These could substantially benefit from remote cooling systems. Such applications can be divided into the following categories:

- Cooling of the devices performing **highly accurate measurements** at low temperatures, for which the cooling source induces mechanical or magnetic disturbances that affect the measurement.
- Cooling needed in **harsh environments**, where the cryocooler can suffer damage due to exposure to excessive magnetic fields or radiation.
- Cooling that needs to be provided in spatially **constrained environments**, where the liquid cryogen usage can be more complex.

The ultra-sensitive Superconducting QUantum Interference Devices (SQUIDs) magnetometers in the CERN Antiproton Decelerator (AD) are one example of the first category. The objective of the AD is to produce antiproton beams and send them to different experiments. It does so by slowing and directing the multitude of secondary particles produced after a beam of protons, coming from the Proton Synchrotron (PS), collides with a block of metal. Since the AD reduces the energy of the beam, its induced electromagnetic field is very low and performing non-perturbing beam diagnostics proves to be a challenge. To address this, a SQUID-based Cryogenic Current Comparator (CCC) has been built, achieving a current resolution of $2.8\,\mathrm{nA}$ [12]. Due to the high sensitivity of the SQUID to mechanical and magnetic interferences, it has to be maintained well-insulated form the surrounding disturbances while operating at very low temperatures. The cooling to achieve these temperatures is provided using a liquid bath of helium at $4.2\,\mathrm{K}$ together with a cryocooler, which is used to re-condense the evaporated helium back into the bath. This configuration is also known as a zero boil-off cryostat. Currently, the curernt signal resolution worsens by a factor of two when the cryostat vacuum pumps used in the system are operating. Studies are currently being conducted to determine if a remote refrigeration would provide an improved and more stable solution in the future.

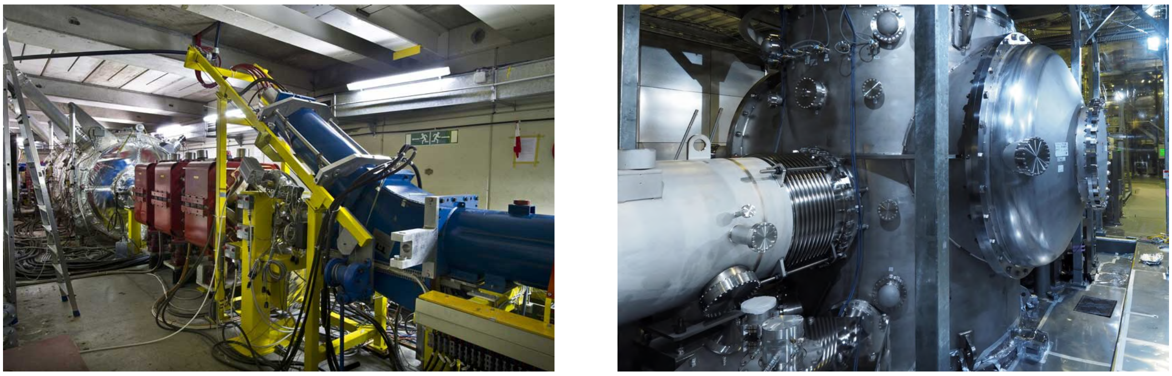

(a) (b)

Figure 2.3: Remote cooling applications examples; (a) CERN's Antiproton Deceleretor (Image: CERN) and (b) KAGRA gravitational wave detector cryostat for the sapphire mirror (Image: KAGRA)

The Kamioka Gravitational Wave Detector (KAGRA) is another example of the first category. The gravitational waves in this case are detected by measuring a distance between two mirror surfaces using a Michelson interferometer. As the distance measurement has to be very precise, even the vibration within the material can disturb the measurement. That is why it was decided to maintain the mirrors at low temperatures. It is very important that no vibrations are induced into the mirrors from the cryocoolers or cryostats. Hence, such project could greatly benefit from remote cooling as well.

As for the second category of applications, an example at CERN would be the High-Radiation to Materials (HiRadMat) Facility [5]. There, material samples and accelerator component assemblies are tested for radiation robustness prior to their installation in the LHC or other high-radiation environments. The facilities use a beam that collides with target metals and produces radiation. If cryocoolers are used, the rare-earth materials inside them get activated after exposure to radiation. As a result, the irradiated cryocoolers can not be used after the experiment since they have to be stored. This situation can also be improved by the means of remote cooling, which would allow the cryocoolers to be located outside of the radiation area.

Lastly, applications such as space or medical treatments, where compactness, size, weight, and autonomy are of paramount importance due to spatial constraints, could greatly benefit from cryocooler-based cooling systems. In space, if the cooling is provided by the means of a cryogen bath where the evaporating cryogen is released, the lifetime of the cooling system becomes limited, affecting the mission. In addition, heavy reservoirs have to be used to store the necessary cryogen. Due to that, a trend towards cryogen-free cooling systems has been established in the space industry [9]. Small particle accelerators for medical application can also benefit from this type of stand-alone turnkey cooling system. These accelerators have an RF cavity which has to be maintained at superconducting state (see. Section 1.2.1). A stand-alone remote cooling system requires almost no maintenance nor cryogen refilling. The following section analyses several architectures for this type of application.

2.3 System studies

A remote cooling system can be implemented through different architectures. The choice, on which one to use, has to be application-dependant since each has its own requirements. In order to know if a specific remote cooling system fits for some purpose, a system study has to be done, where different alternatives are analysed and their performance is compared to the set requirements. The purpose of this section is to explain the followed methodology for the performed system studies, and to show the obtained results. The focus will be on the cooling power at different temperatures, mass flows and heat exchanger effectivenesses. The chosen application is an RF cavity cooling, but both the results and the procedure can be extrapolated to other similar cases.

Fig. 2.4 shows the three architectures that are studied and compared. They all have a main cryostat where the cryocooler and most of the circulation system are located, and a remote cryostat, with the CIF. The three designs use the same two-stage cryocooler, a PT420 [18], with its performance map measured experimentally depicted in Fig. 2.5. This map shows the evolutions of the cryocooler stage temperatures for the different

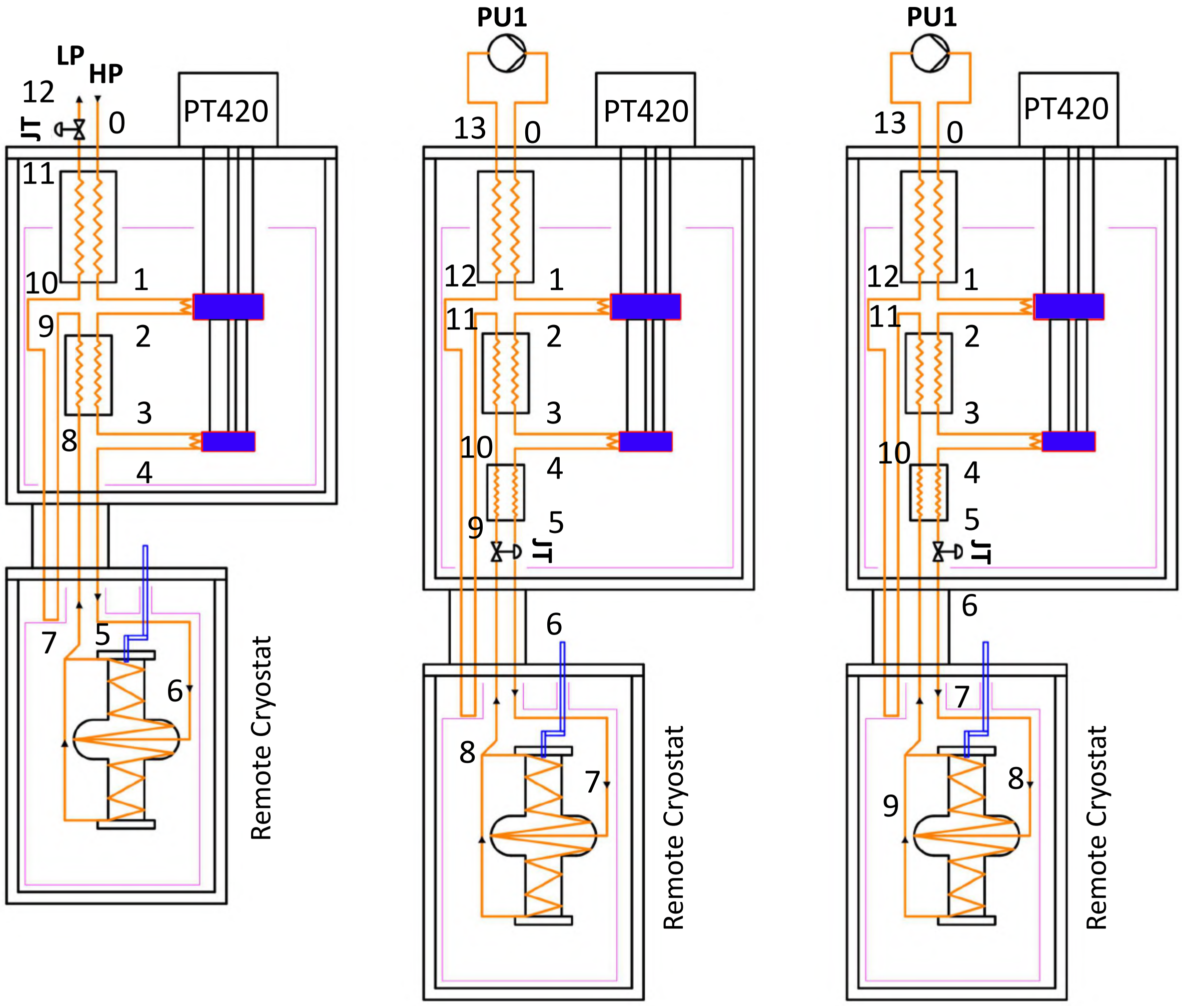

Figure 2.4: Three cryocooler-based remote cooling architectures for an RF cavity cooling. Cryocooler: two-stage (in blue) pulse-tube, model PT420 from Cryomech; (a) System 1: HP flow at 25 bar from the cryocooler's compressor is pre-cooled in the HEXs and delivered to the remote cooling location, (b) System 2: the flow is circulated using pump (PU1), pre-cooled and delivered to the remote CIF. JT restriction downstream the CIF is used to increase the pre-cooling in CFHEX 3, (c) System 3: the flow is circulated using pump (PU1), pre-cooled and delivered to the remote CIF. JT restriction upstream the CIF is used to increase the cooling power at the remote location and create a two-phase flow for stable temperature condition at the CIF. For all three systems, the blue line surrounding the cryocooler and the convection loop represents the radiation shield. This shield is thermalysed at the cryocooler's first stage temperature with a pipe between points 9-10 for system 1, and 11-12 for System 2 and 3.

amounts of power deposited at each stage. The expected cooling power is deduced from the second stage, for instance, $10\,\mathrm{W}$ at $11\,\mathrm{K}$ or $2\,\mathrm{W}$ at $4.5\,\mathrm{K}$.

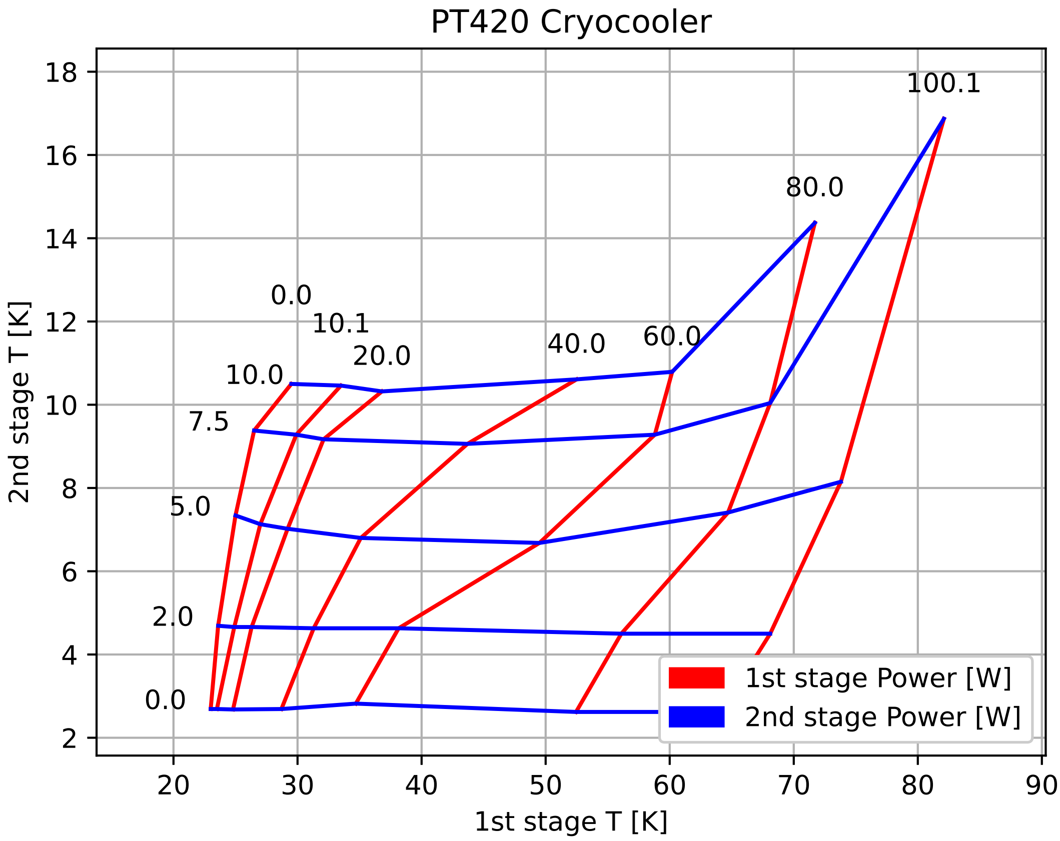

Figure 2.5: PT420 cryocooler performance map measured experimentally. Red and blue lines represent the powers that can be deposited at each stage at the corresponding temperatures.

The behaviour of the cryocooler has not been measuered and is hence not known outside of the defined area in Fig. 2.5 map. Therefore, operation there should be avoided as well as in the unstable regions of the map, i.e., wherever there is an abrupt change in one of the stage temperatures while the other one only changes slightly.

The interface between the CIF and the cold helium can be accomplished in different configurations. For the RF cavity cooling, the heat needs to be extracted in a uniform manner to ensure a homogeneous temperature distribution on the surface of the cavity. This can be ensured via the use of a capillary as shown in the arrangements in Fig. 2.4.

2.3.1 Thermal radiation heat loads analysis

A common characteristic of the three alternatives is the cooling of both the main and the remote cryostats. The cryostat consists of several layers. The outermost one is a vacuum chamber. Vacuum space is used to ensure that heat from the outside is not transferred to the cold interfaces of the set-up by convection. In addition, air, if present, would condense on the cold faces inside the cryostat creating additional heat loads and introducing safety risks. Inside the vacuum chamber there is a radiation shield, which is a cylinder made out of copper surrounded by a Multi-Layer Insulation (MLI) (see Fig. 3.9). The intention behind this combination is to reduce as much as possible radiation heat flux from the warm surfaces. Otherwise, cooling power at the cryocooler stages would be lost absorbing this heat load.

The vacuum chamber is at room temperature, but it is thermally decoupled from the cold parts of the setup including the cryocooler stage and the shield. Thus, the heat transfer to the cold parts by conduction is reduced. The copper shield is covered with MLI blankets in order to reduce the effective radiation transmission. Next, the parasitic heat that makes it to the cold side of the MLI insulation is absorbed by the copper shield, which is being held at $\sim$55 K. In between points 9-10 for the first system and 11-12 for the second and the third one, the returning cold fluid flow is re-directed to pre-cool the thermal radiation shields enveloping the main and remote cryostats. The reason to make the radiation shield out of copper is to cool it down uniformly thanks to its great thermal conductivity. The flow for the shield pre-cooling is taken at the mentioned locations because they are at the height of the first stage so that eventually, it is the first stage of the cryocooler that absorbs the heat loads.

Before going into the detail of each system, a common calculation for the radiation loads on the copper shield is performed. Even though the first system is slightly smaller, the cryostats were assumed to have the same size since the difference should be minimal and not impact significantly the conclusions. Both the main and the remote cryostat are assumed to have a cylindrical shape of diameter ϕ, a height H, a lateral area $A_{lateral}$ and a lids area A_{lids}, as per Tab. 2.1.

	$\phi[m]$	H [m]	$A_{lateral}[m^2]$	$A_{lids}[m^2]$	Numb. of shield MLI layers
Main Cryostat	0.6	1	1.89	0.56	20
Remote Cryostat	0.3	0.5	0.47	0.14	20

Table 2.1: Dimensions of the main and remote cryostats used for calculations of the radiation heat load on the thermal shield.

To find the heat load that has to be evacuated from each radiation shield, the resultant heat load originating at the vacuum chamber walls has to be calculated taking into account the distance between the surfaces in the vacuum and the protective MLI. A simplified method can be defined considering an apparent thermal conductivity $\lambda_{apparent}$ or an effective radiation emissivity ϵ_{eff} that includes the combination of vacuum with N layers of MLI. This can be done thanks to some experimental data obtained for this specific number of MLI layers. A more detailed analytical approach can prove to be difficult due to the variations in performance of MLI insulation at different pressures. Hence, for a vacuum pressure under 1×10^{-4} mbar and for 20 layers of MLI [3]:

- $\lambda_{apparent} = 2.4 \times 10^{-3}\,\mathrm{W\,mK^{-1}}$
- $\epsilon_{eff} = 1.3 \times 10^{-3}$

Using those values, the heat flow $\dot{Q}$ can easily be calculated using one of the following equations:

$$\dot{Q} = \lambda_{apparent} A_{total}(T_w - T_c) \tag{2.12}$$

$$\dot{Q} = \epsilon_{eff}\sigma A_{total}(T_w^4 - T_c^4) \tag{2.13}$$

Where A_{total} is the sum of $A_{lateral}$ and A_{lids}, T_w and T_c are the warm-end and cold-end temperature respectively, and σ is the Stefan-Boltzmann constant.

It is assumed that the vacuum chamber is at room temperature ($T_w = 295\,\mathrm{K}$) and that the radiation shield is at the temperature of the cryocooler's first stage ($T_c = 50\,\mathrm{K}$). With that in mind, equation (2.12) is solved for both shields:

- $\boldsymbol{\dot{Q}_{main} = 1.44\,\mathrm{W}}$
- $\boldsymbol{\dot{Q}_{remote} = 0.36\,\mathrm{W}}$

Similar values would be obtained if eq. (2.13) was used. These results will be taken into account later on during the system studies.

There is one more heat load to be extracted by the circulation system for the use case of an RF cavity cooling. Between points 5-6 on System 1, 6-7 on System 2 and 7-8 on System 3, there is an incoming heat flow from the RF cable that has to be intercepted. The largest part will be extracted by the shield ($\dot{Q}_{RF_{shield}}$), where the RF cable will be thermalised. However, a small portion will be added to the passing helium ($\dot{Q}_{RF_{HE}}$). The following empirical values, based on the Cryolab experience, where used for the system simulation.

- $\boldsymbol{\dot{Q}_{RF_{shiled}} = 2\,\mathrm{W}}$
- $\boldsymbol{\dot{Q}_{RF_{HE}} = 0.02\,\mathrm{W}}$

Once the radiation heat loads are evaluated, the system analysis needs to be performed in order to evaluate the cooling power that each of the options in Fig. 2.4 could provide. To proceed, a number of assumptions needs to be made:

- Isenthalpic expansion in the JT-valve.
- Pressure drops across the different heat exchangers are assumed to be known. A value of 100 mbar is assumed for each CFHEX stream and 75 mbar for the HEX at each of the cryocooler stages.
- The effectiveness of the HEX at the stages is assumed to be 95 %. The effectiveness of the CFHEXs is a study parameter and its influence on the system performance will be analysed.
- Helium pressure at the outlet of the cooling loop of Systems 2 and 3, is assumed to be 1 bar. This implies that the fluid pressure at point 8 and 9, respectively, is 1.3 bar.

Using these assumptions, the performance of each system can be evaluated based on the known fluid inlet temperatures, pressures, mass flow rates and the cryocooler performances. The analysis methodology for the three systems is similar, however certain particularities apply depending on specific features of the systems, e.g. JT-expansion. The system calculations are based on a system of simultaneous equations where the unknowns are the enthalpies at each point. Those are composed using the effectiveness formulas of each heat-exchanger, the initial conditions, the isenthalpic considerations and the radiation heat loads. The system is then solved iteratively. Initially, a constant pressure is assumed along the entire fluid circuit. This assumption gives enthalpies values which are relatively close to the final solution, hence, the number of iterations necessary for convergence will decrease.

2.3.2 High-pressure System (1)

The first cooling arrangement to be analysed is shown in Fig. 2.4a. The particularities of this architecture are the following:

- High pressure input of 25 bar, taken from the cryocooler supply helium line[2].
- High pressure output of 8 bar, merging into the cryocooler return line.
- Two CFHEX.

[2]The cryocooler is supplied with helium at high pressures. Using the same fluid line for the circulation circuit reduces the amount of equipment needed. However, this line introduces vibrations due to the nature of the cryocooler.

- The interest is to keep the pressure as high as possible during the cooling in order to reduce vibrations, which is a result of the flow having a low velocity inside a high pressures circulation loop. Hence, the JT-valve is located at the system outlet and is only there to reduce the pressure of the flow to 8 bar and set the mass flow rate value.

The main advantages of this configuration are:

- Reduced vibration.
- Less equipment needed. No additional circulation pump is required and nether is one of the three CFHEX that is present in the other options.
- The higher operating pressure at the CIF enables the use of smaller capillary tubes. This is beneficial for integration purposes, as the cooling can be more uniformly distributed across the CIF.

The conditions are known at point 0 in Fig. 2.4a:

$$h_0 = h(t_0, p_0) = h(295\,\text{K}, 25\,\text{bar}) = h_{in} \tag{2.14}$$

The effectivenesses ϵ_{H_1} and ϵ_{H_2} of the two counter-flow heat exchangers from Fig. 2.4 yields the following expressions obtained from [2]:

$$\epsilon_{H_1} = \frac{h_0 - h_1}{\min\left(h_0 - h(T_{10}, p_1), h(T_0, p_{11}) - h_{10}\right)} = \frac{h_{11} - h_{10}}{\min\left(h_0 - h(T_{10}, p_1), h(T_0, p_{11}) - h_{10}\right)} \tag{2.15}$$

$$\epsilon_{H_2} = \frac{h_2 - h_3}{\min\left(h_2 - h(T_8, p_3), h(T_2, p_9) - h_8\right)} = \frac{h_9 - h_8}{\min\left(h_2 - h(T_8, p_3), h(T_2, p_9) - h_8\right)} \tag{2.16}$$

Where the subscripts refer to the locations in Fig. 2.4a. An effectiveness, ϵ_{S_1} and ϵ_{S_1}, for the heat exchangers at the cryocooler stages can also be defined. In an ideal heat exchanger the temperature of the fluid at the outlet is the same as that of the cryocooler stage. Based on this, the effectivenesses have been defined as follows:

$$\epsilon_{S_1} = \frac{h_1 - h_2}{h_1 - h(T_{S1}, p_2)} \tag{2.17}$$

$$\epsilon_{S_2} = \frac{h_3 - h_4}{h_3 - h(T_{S2}, p_4)} \tag{2.18}$$

The temperatures at each stage, T_{S_1} and T_{S_2}, are obtained using the cryocooler performance map from Fig. 2.5, where the power at the stages is given by the difference in enthalpies of the flow between the inlet and the outlet of the HEX.

The JT-valve provides an isenthalpic expansion. Hence:

$$h_{11} = h_{12} \tag{2.19}$$

Also, there are several points that are considered isenthalpic since no work nor heat is applied and the pressure drop is negligible. We have this situation between points 4-5 and 7-8 in Fig. 2.4a.

$$h_5 = h_4 \tag{2.20}$$

$$h_8 = h_7 \tag{2.21}$$

For the capillary cooling at the RF cavity, the heat exchange is defined according to the heat load:

$$h_7 - h_6 = \frac{\dot{Q}_{load}}{\dot{m}} \tag{2.22}$$

Where $\dot{m}$ is the mass flow rate of the fluid. $\dot{Q}_{load}$ is an input for the simulation and represents the cooling power at the CIF. The interest is to calculate the temperature of the cooled device at each cooling power and for a range of mass flow rates.

Finally, as explained at the start of this section, between points 5-6 and 9-10, helium is used to thermalise the RF cable and the vacuum chamber respectively. It is considered that this happens at a constant pressure. Hence:

$$h_6 - h_5 = \frac{\dot{Q}_{5-6}}{\dot{m}} = \frac{\dot{Q}_{RF_{HE}}}{\dot{m}} \tag{2.23}$$

$$h_{10} - h_9 = \frac{\dot{Q}_{9-10}}{\dot{m}} = \frac{\dot{Q}_{RF_{shield}} + \dot{Q}_{main} + \dot{Q}_{remote}}{\dot{m}} \tag{2.24}$$

Combining equations 2.14-2.24 gives a system of 13 equations, which have as unknowns the enthalpies at each point. That system can be simplified for the first iteration if constant pressure throughout the fluid loop is considered. This simplification yields the following matrix equation:

$$\begin{bmatrix} 1 & 0 & 0 & 0 & 0 & 0 & 0 & 0 & 0 & 0 & 0 & 0 & 0 \\ 0 & -1 & 0 & 0 & 0 & 0 & 0 & 0 & 0 & 0 & \epsilon_{H_1} & 0 & 0 \\ 0 & \epsilon_{S_1}-1 & 1 & 0 & 0 & 0 & 0 & 0 & 0 & 0 & 0 & 0 & 0 \\ 0 & 0 & \epsilon_{H_2}-1 & 1 & 0 & 0 & 0 & 0 & -\epsilon_{H_2} & 0 & 0 & 0 & 0 \\ 0 & 0 & 0 & \epsilon_{S_2}-1 & 1 & 0 & 0 & 0 & 0 & 0 & 0 & 0 & 0 \\ 0 & 0 & 0 & 0 & -1 & 1 & 0 & 0 & 0 & 0 & 0 & 0 & 0 \\ 0 & 0 & 0 & 0 & 0 & -1 & 1 & 0 & 0 & 0 & 0 & 0 & 0 \\ 0 & 0 & 0 & 0 & 0 & 0 & -1 & 1 & 0 & 0 & 0 & 0 & 0 \\ 0 & 0 & 0 & 0 & 0 & 0 & 0 & -1 & 1 & 0 & 0 & 0 & 0 \\ 0 & 0 & \epsilon_{H_2} & 0 & 0 & 0 & 0 & 0 & -\epsilon_{H_2}+1 & -1 & 0 & 0 & 0 \\ 0 & 0 & 0 & 0 & 0 & 0 & 0 & 0 & 0 & -1 & 1 & 0 & 0 \\ 0 & 0 & 0 & 0 & 0 & 0 & 0 & 0 & 0 & 0 & 1-\epsilon_{H_1} & -1 & 0 \\ 0 & 0 & 0 & 0 & 0 & 0 & 0 & 0 & 0 & 0 & 0 & -1 & 1 \end{bmatrix} \begin{bmatrix} h_0 \\ h_1 \\ h_2 \\ h_3 \\ h_4 \\ h_5 \\ h_6 \\ h_7 \\ h_8 \\ h_9 \\ h_{10} \\ h_{11} \\ h_{12} \end{bmatrix} = \begin{bmatrix} h_{in} \\ \epsilon_{H_1} h_{in} - h_{in} \\ \epsilon_{S_1} h(T_{s1}, p_2) \\ 0 \\ \epsilon_{S_2} h(T_{s2}, p_4) \\ 0 \\ \dot{Q}_{6-5}/\dot{m} \\ \dot{Q}_{7-6}/\dot{m} \\ 0 \\ 0 \\ \dot{Q}_{10-9}/\dot{m} \\ -\epsilon_{H_1} h_{in} \\ 0 \end{bmatrix} \quad (2.25)$$

Its solution would give an initial estimation of the enthalpies at each point. Next, since the pressures are known at each point, the temperatures can be deduced. With these values the iterative process of solving equations (2.14)-(2.24) can start without any additional assumption. The final enthalpies are obtained once the convergence criteria are satisfied between two consecutive iterations.

2.3.3 Low-pressure two-phase flow System (3)

The second cooling arrangement to be calculated is shown in Fig. 2.4c. The particularities of this architecture are the following:

- Independent pump, providing 5 bar fluid flows to the HP side of the loop, and accepting 1 bar from the LP side of the system.
- JT-valve before the cooled device, creating a two-phase flow on the CIF, which implies that temperature is kept constant there.

The following advantages are gained with this configuration:

- While vibrations at the CIF are higher than System 1 or 2, having a constant temperature along the CIF can ensure that the behaviour of the system is more predictable.
- The cooling power may be increased thanks to the JT cooling effect.

Again, the resolution procedure is very similar. The conditions are known at point 0:

$$h_0 = h(t_0, p_0) = h(295\,\mathrm{K}, 5\,\mathrm{bar}) = h_{in} \quad (2.26)$$

The same effectiveness definition for both the counter-flow and the cryocooler stages heat exchangers as in the previous system is used. Also, between points 6-7 the process is considered isenthalpic.

Now, the JT-valve provides an isenthalpic expansion right before the CIF. Hence:

$$h_6 = h_5 \tag{2.27}$$

For the capillary at the RF cavity, it is assumed that at point 9, that is, after the cooled device, the fluid is in saturated vapour conditions. Hence, its corresponding enthalpy h_{sv} is imposed.

$$h_9 = h_{sv}(p_9) \tag{2.28}$$

This enforces the two-phase flow at the CIF. As a result, the cooling power of the system can become and output of the analysis. Thus, its temperature will correspond to helium saturation temperature at p_9. Consequently, the cooling power can be calculated as a function of the mass flow rate.

As in system 1, between the points 7-8 and 11-12, the helium is used to thermalise the RF cable $\dot{Q}_{RF_{HE}}$ and the vacuum chamber $\dot{Q}_{11-12}$ respectively. The same values apply for this case.

Assuming constant pressure along the system for the first iteration and combining the previous relations yields the matrix eq. (2.29).

$$\begin{bmatrix}
1 & 0 & 0 & 0 & 0 & 0 & 0 & 0 & 0 & 0 & 0 & 0 & 0 & 0 \\
\epsilon_{H_1}-1 & 1 & 0 & 0 & 0 & 0 & 0 & 0 & 0 & 0 & 0 & 0 & -\epsilon_{H_1} & 0 \\
0 & \epsilon_{S_1}-1 & 1 & 0 & 0 & 0 & 0 & 0 & 0 & 0 & 0 & 0 & 0 & 0 \\
0 & 0 & \epsilon_{H_2}-1 & 1 & 0 & 0 & 0 & 0 & 0 & 0 & -\epsilon_{H_2} & 0 & 0 & 0 \\
0 & 0 & 0 & \epsilon_{S_2}-1 & 1 & 0 & 0 & 0 & 0 & 0 & 0 & 0 & 0 & 0 \\
0 & 0 & 0 & 0 & \epsilon_{H_3}-1 & 1 & 0 & 0 & 0 & -\epsilon_{H_3} & 0 & 0 & 0 & 0 \\
0 & 0 & 0 & 0 & 0 & -1 & 1 & 0 & 0 & 0 & 0 & 0 & 0 & 0 \\
0 & 0 & 0 & 0 & 0 & 0 & -1 & 1 & 0 & 0 & 0 & 0 & 0 & 0 \\
0 & 0 & 0 & 0 & 0 & 0 & 0 & -1 & 1 & 0 & 0 & 0 & 0 & 0 \\
0 & 0 & 0 & 0 & 0 & 0 & 0 & 0 & 0 & 1 & 0 & 0 & 0 & 0 \\
0 & 0 & 0 & 0 & \epsilon_{H_3} & 0 & 0 & 0 & 0 & 1-\epsilon_{H_3} & -1 & 0 & 0 & 0 \\
0 & 0 & \epsilon_{H_2} & 0 & 0 & 0 & 0 & 0 & 0 & 0 & 1-\epsilon_{H_2} & -1 & 0 & 0 \\
0 & 0 & 0 & 0 & 0 & 0 & 0 & 0 & 0 & 0 & 0 & -1 & 1 & 0 \\
\epsilon_{H_1} & 0 & 0 & 0 & 0 & 0 & 0 & 0 & 0 & 0 & 0 & 0 & 1-\epsilon_{H_1} & -1
\end{bmatrix}
\begin{bmatrix} h_0 \\ h_1 \\ h_2 \\ h_3 \\ h_4 \\ h_5 \\ h_6 \\ h_7 \\ h_8 \\ h_9 \\ h_{10} \\ h_{11} \\ h_{12} \\ h_{13} \end{bmatrix}
=
\begin{bmatrix} h_{in} \\ 0 \\ \epsilon_{S_1} h(T_{s1}, p_2) \\ 0 \\ \epsilon_{S_2} h(T_{s2}, p_4) \\ 0 \\ 0 \\ 0 \\ \dot{Q}_{7-8}/\dot{m} \\ h_{sv}(p_9) \\ 0 \\ 0 \\ \dot{Q}_{11-12}/\dot{m} \\ 0 \end{bmatrix} \tag{2.29}$$

The final enthaply distribution is obtained following the same procedure as described in Sec. 2.3.2.

2.3.4 Low-pressure single-phase flow System (2)

Finally, the last arrangement to be analysed is the one depicted in Fig. 2.4b. The particularities of this architecture are the following:

- Independent pump, providing 5 bar fluid flows to the HP side of the loop, and accepting 1 bar from the LP side of the system.
- The JT-valve is located after the CIF, increasing the pre-cooling from the CFHEX3. This ensures that lower temperature is achieved at the CIF, while a single-phase flow is kept.

Advantages of this configuration is that it is a hybrid approach between System 1 and 3. The resultant cooling power provided by the system is expected to be higher than that of System 1, and compared to System 3, vibrations are reduced due to the single-phase flow at the CIF.

Effectiveness definitions, isenthalpic process considerations and heat load and thermalisation loads assumptions from System 1 are also used here. The initial conditions are the same as in System 3 (see Eq. (2.26)), as both systems use the same independent circulation pump.

In this case, the JT-valve provides an isenthalpic expansion between points 9 and 10, in Fig. 2.4b , right after the CIF. The resulting system of equations for the enthalpies and for the same constant pressure assumption is the following:

$$\begin{bmatrix}
1 & 0 & 0 & 0 & 0 & 0 & 0 & 0 & 0 & 0 & 0 & 0 & 0 & 0 \\
\epsilon_{H_1}-1 & 1 & 0 & 0 & 0 & 0 & 0 & 0 & 0 & 0 & 0 & 0 & -\epsilon_{H_1} & 0 \\
0 & \epsilon_{S_1}-1 & 1 & 0 & 0 & 0 & 0 & 0 & 0 & 0 & 0 & 0 & 0 & 0 \\
0 & 0 & \epsilon_{H_2}-1 & 1 & 0 & 0 & 0 & 0 & 0 & 0 & -\epsilon_{H_2} & 0 & 0 & 0 \\
0 & 0 & 0 & \epsilon_{S_2}-1 & 1 & 0 & 0 & 0 & 0 & 0 & 0 & 0 & 0 & 0 \\
0 & 0 & 0 & 0 & \epsilon_{H_3}-1 & 1 & 0 & 0 & 0 & -\epsilon_{H_3} & 0 & 0 & 0 & 0 \\
0 & 0 & 0 & 0 & 0 & -1 & 1 & 0 & 0 & 0 & 0 & 0 & 0 & 0 \\
0 & 0 & 0 & 0 & 0 & 0 & -1 & 1 & 0 & 0 & 0 & 0 & 0 & 0 \\
0 & 0 & 0 & 0 & 0 & 0 & 0 & -1 & 1 & 0 & 0 & 0 & 0 & 0 \\
0 & 0 & 0 & 0 & 0 & 0 & 0 & 0 & -1 & 1 & 0 & 0 & 0 & 0 \\
0 & 0 & 0 & 0 & \epsilon_{H_3} & 0 & 0 & 0 & 0 & 1-\epsilon_{H_2} & -1 & 0 & 0 & 0 \\
0 & 0 & \epsilon_{H_2} & 0 & 0 & 0 & 0 & 0 & 0 & 0 & 1-\epsilon_{H_2} & -1 & 0 & 0 \\
0 & 0 & 0 & 0 & 0 & 0 & 0 & 0 & 0 & 0 & 0 & -1 & 1 & 0 \\
\epsilon_{H_1} & 0 & 0 & 0 & 0 & 0 & 0 & 0 & 0 & 0 & 0 & 0 & 1-\epsilon_{H_1} & -1
\end{bmatrix}
\begin{bmatrix} h_0 \\ h_1 \\ h_2 \\ h_3 \\ h_4 \\ h_5 \\ h_6 \\ h_7 \\ h_8 \\ h_9 \\ h_{10} \\ h_{11} \\ h_{12} \\ h_{12} \end{bmatrix}
=
\begin{bmatrix} h_{in} \\ 0 \\ \epsilon_{S_1} h(T_{s1}, p_2) \\ 0 \\ \epsilon_{S_2} h(T_{s2}, p_4) \\ 0 \\ 0 \\ \dot{Q}_{6-7}/\dot{m} \\ \dot{Q}_{load}/\dot{m} \\ 0 \\ 0 \\ 0 \\ \dot{Q}_{11-12}/\dot{m} \\ 0 \end{bmatrix}
\tag{2.30}$$

The final enthalpy distribution is obtained following the same procedure as described in Sec. 2.3.2.

2.3.5 Results

System 1 and 2 from Fig. 2.4 provide a different cooling power for each temperature[3] at the CIF since they do not operate in the two-phase region. The obtained results are represented in Fig. 2.6 and 2.7. In both cases, the effectiveness values of all the CFHEXs have been set to 95 %. The heat map presents the temperature of the CIF for different cooling powers at different mass flow rates. The curves are showing the temperature profile for three representative chosen cooling powers for different mass flow rates. The profiles indicate that there is a minimum temperature that can be achieved for a specific mass flow rate under a given heat load. Moreover, higher required cooling power implies higher CIF temperatures for System 1. System 2 shows no optimum. It is limited to the cryocooler cooling performance, given by the respective maximum mass flow rate. Next, Fig.2.8a compares the performance of System 1 and 2 for the same cooling power. It shows that System 2 achieves considerably lower temperatures, with a minimum difference of 2 K. However, System 2 is limited at high cooling powers with a maximum cooling power of 2 W and at low mass flow rates, not being able to operating below 100 $\mathrm{mg\,s^{-1}}$. These limitations appear because at high cooling powers or at low mass flow rates, the circuit is not able to get into the two-phase area. On the contrary, it starts drifting in temperature due to the fact that now, the coldest point of the circuit is right after the second stage, and not along the cooled device. System 1, on the other hand, can reach cooling powers up to 5 W at about 10 K at the CIF (see Fig. 2.6b).

On the other hand, System 3 operates in the two-phase region along the CIF. Since the fluid pressure is fixed downstream of the CIF, so is the temperature for the helium at saturation conditions at 1.3 bar, thus 4.5 K (see Sec. 2.3.3 for assumptions). Therefore, the plot in Fig. 2.8b) is sufficient to characterise its behaviour. It gives the cooling power at a CIF temperature of 4.5 K for different mass flow rates for three effectiveness values for the CFHEXs. The cooling power increases linearly at low mass flow rates. When high mass flow rates are reached, the trend slows down. For 93 % effectiveness, a maximum cooling power is reached at 240 $\mathrm{mg\,s^{-1}}$. Optimum mass flow rates for higher CFHEX effectiveness could be found by simulating a larger range of mass flow rates. For the simulated values, the maximum achievable cooling power increases from 2.8 W for 93 % to 3.9 W for 98 %. Despite of that, operating at the highest mass flow rate is not always the best scenario since it implies more heat load in the cryocooler stages, which in turn implies higher stage temperatures. As seen in Fig. 2.5, such an operation point is closer to the limits of the cryocooler, hence providing a less stable operation. When compared with System 1 and 2, System 3 offers the best cooling power to CIF temperature ratio, surpassing 3 W at 4.5 K.

[3] The temperature along the CIF is not constant, but increases along its length. For the sake of simplification, an average of the temperature along the CIF is presented in the results and in the graphs. However, for the analysis, a linearly increasing profile is considered.

Concluding, if vibrations are critical while low temperature is not that important, System 1 would be the desirable approach as it proves to be more robust than System 2. If, on the contrary, vibrations are not that critical but low temperature is needed, then system 3 would be the best approach. Finally, System 2 is dropped from further consideration due to its lack of robustness.

2.4 The need for an improved CFHEX design

The effectiveness of the involved heat exchangers has been shown to have a big impact on the performance and viability of the remote cooling system, as seen from Fig. 2.8b. Very high values are required for a good transport of the cooling power from the cold head of the cryocooler to the cooled device. During the analysis, it was found that the minimum effectiveness for System 3 to achieve a useful cooling power above 0 W at the CIF is 93 %, hence the goal to develop a CFHEX with a minimum effectiveness of 95 % was set.

Fig. 2.8b shows that about 35 % increase in cooling power of the system is achieved for an increase of 5 % in the effectiveness of the CFHEX. Hence, it is clear that the performance of the CFHEX is correlated and is very relevant to the performance of the remote cooling system. This, added to the further potential of remote cooling systems, justifies the need to do further research into improving the CFHEX effectiveness value with a more sophisticated design.

In this context, novel counter-flow heat exchangers are under design and development at the Cryolab, aiming to develop compact high-effectiveness (>95 %) heat exchanger and/or to establish a reliable manufacturing procedures and methods for its commissioning.

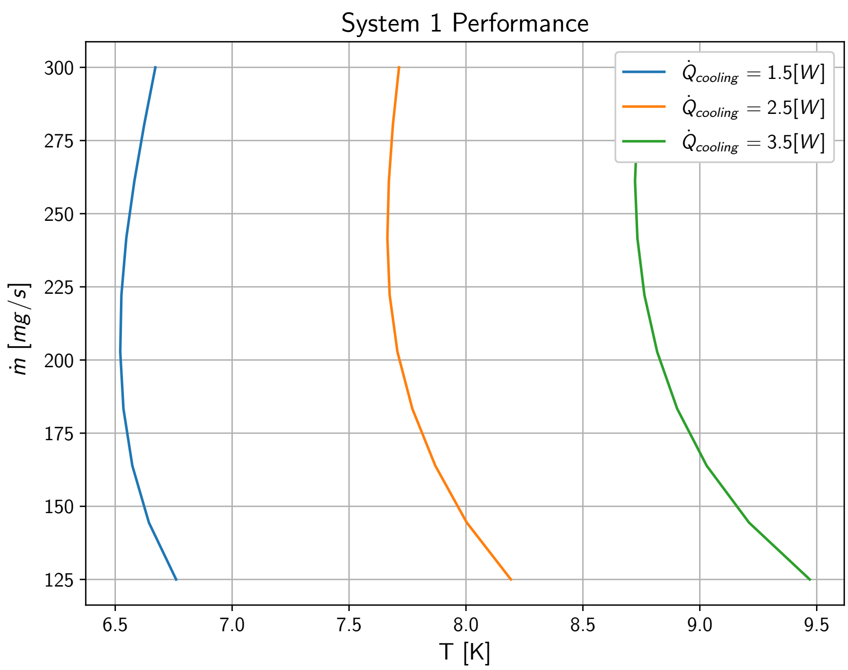

(a)

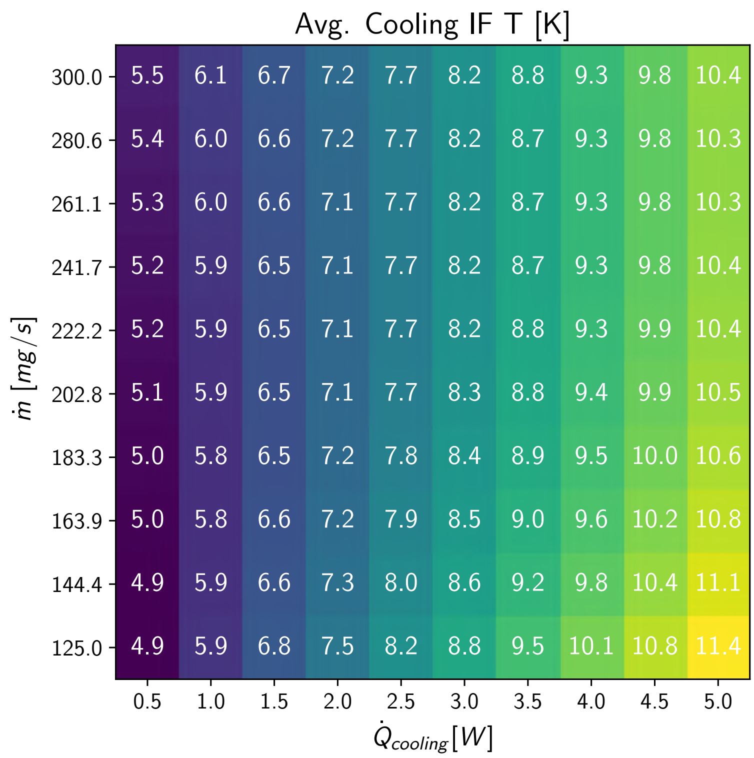

(b)

Figure 2.6: Performance of System 1; (a) shows the temperature profiles for a range of mass flow rates at three selected cooling powers. Each profile presents an optimum $\dot{m}$ that gives the lower CIF temperature and (b) heat map that includes all the simulated cooling powers.

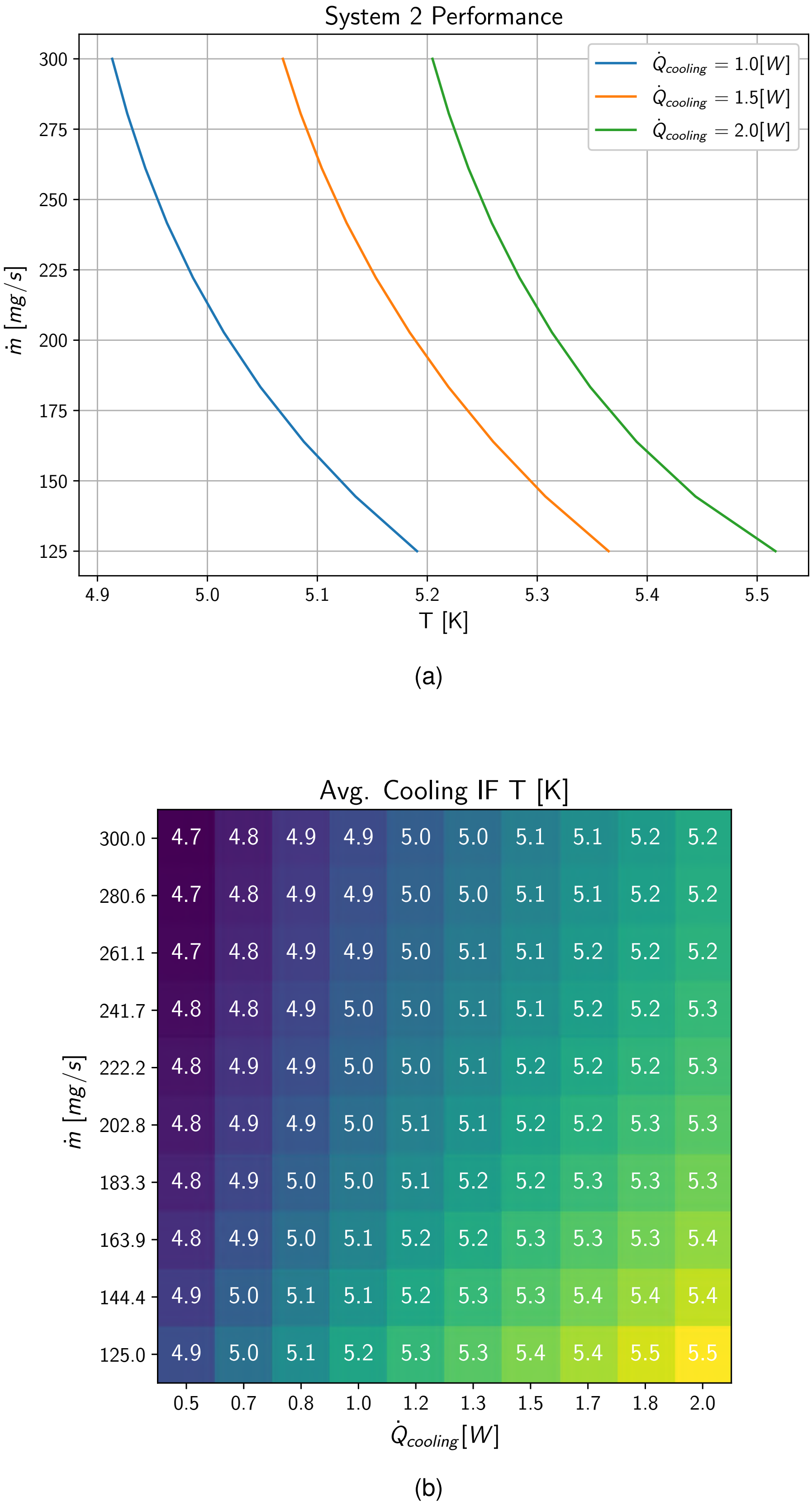

Figure 2.7: Performance of System 2; (a) shows the temperature profiles for a range of mass flow rates at three selected cooling powers; (b) heat map that includes all the simulated cooling powers.

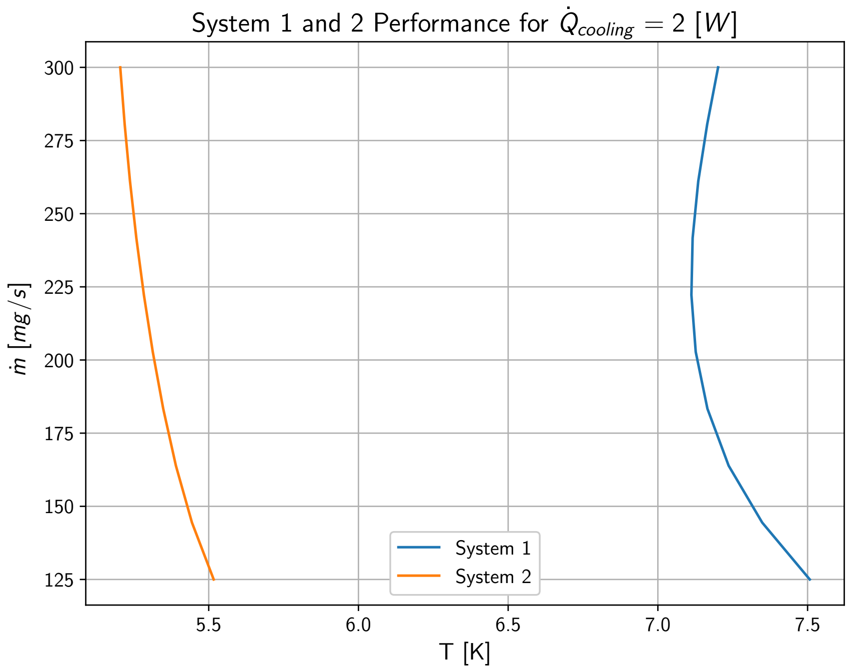

(a)

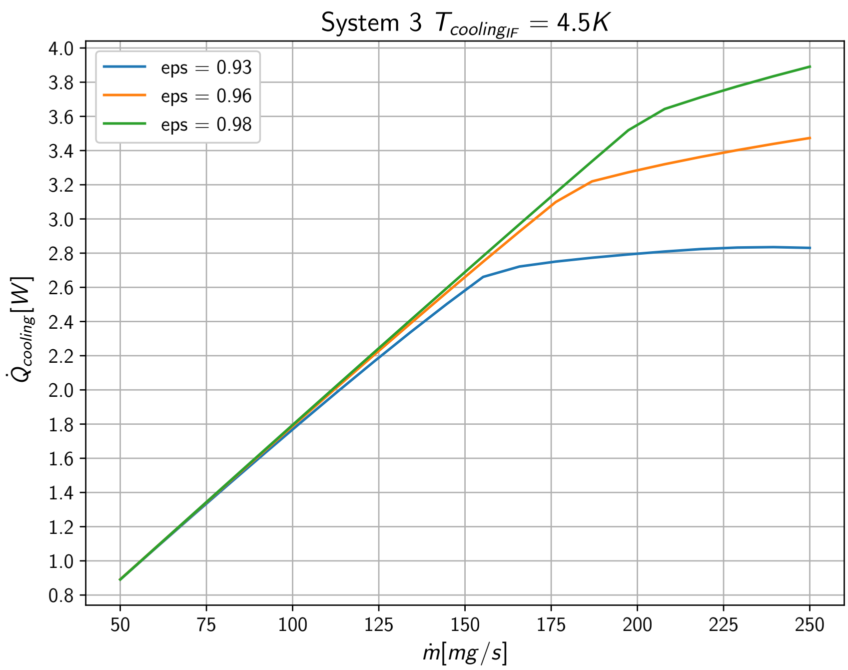

(b)

Figure 2.8: (a) Performance comparison between System 1 and 2 for a fixed cooling power of 2 W. For the selected range, System 2 reaches lower temperatures for the same mass flow rates; and (b) performance of System 3 showing its cooling power for different mass flow rates and effectiveness values. The gain in performance reaches 35 % for 250 mg s^{-1} between 93 % and 98 %.

Chapter 3

Heat exchanger characterisation

3.1 State at the beginning of the internship

A remote cooling system is composed of several heat exchangers that serve the purpose of pre-cooling the flow. As demonstrated in Sec. 2.4, they are critical components for the entire system to maximise and deliver the cooling power to a remote location.

Aleksandra Onufrena is a doctoral student at the Cryolab. Her PhD is about the design of a compact highly effective heat exchanger. She has developed a numerical model of the HEX, and she aims to validate it experimentally. The plan is to use a generic remote cooling system as depicted in Fig. 3.1, to test and measure the performance of the numerically analysed, designed, and manufactured heat exchanger. The remote cooling system from Fig. 3.1 allows for an incremental and iterative CFHEX design since it uses three heat exchangers. The first step would be to make a remote cooling system composed of only one heat exchanger. CFHEX1, would be the first design iteration. A measurement campaign can be accomplished at this point in order to characterise the behaviour and the performance of CFHEX1. Specific improvements could be proposed using the obtained results. These would enable a second CFHEX design, which can be consequently implemented as the CFHEX2 of the remote cooling system, as shown in Fig. 3.6. The process would be repeated until the three counter-flow heat exchangers are integrated. The reason that three CFHEXs are used is because they are only useful before the first and the second stage of the cryocooler, and before the CIF. Also, the third CFHEX is only needed when the JT configuration is used, as the combination of both increases the cooling that the JT-valve would provide on its own. As long as a two-stage cryocooler is used, more CFHEXs would be equivalent to making one of the CFHEX longer, which helps increasing its effectiveness, but results in higher pressure drops. Therefore, a trade-off needs to be made according to the application in order to optimise the design.

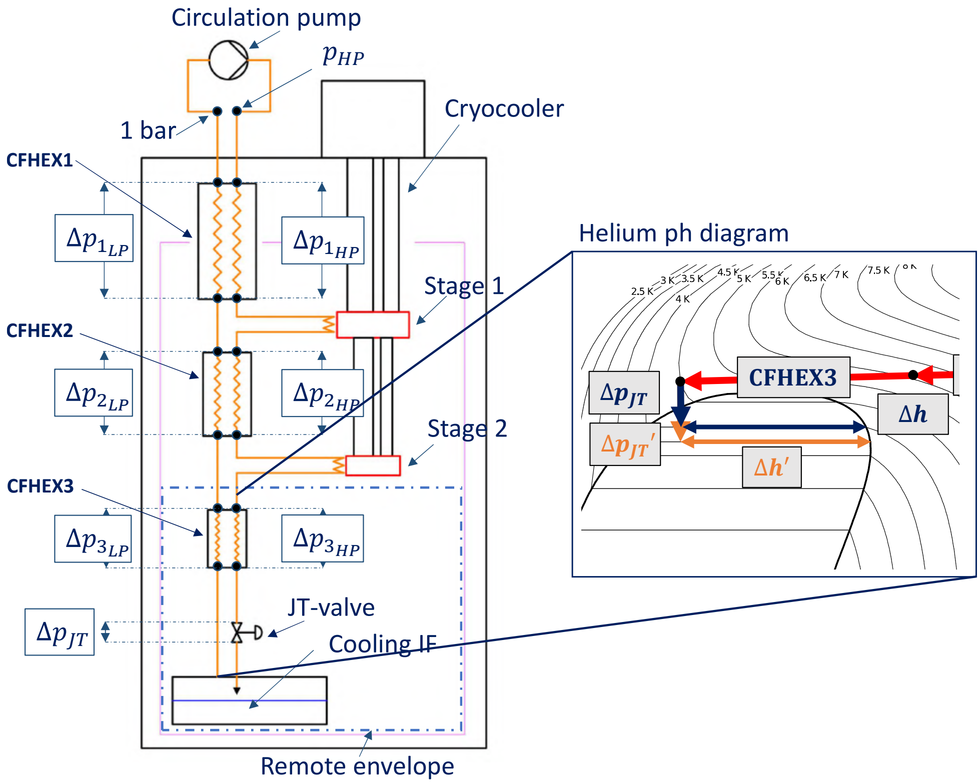

Figure 3.1: Schematic circuit of the heat exchangers CFHEX1, CFHEX2 and CFHEX3 of the chosen remote cooling architecture and their respective HP ($\Delta p_{1_{HP}}$, $\Delta p_{2_{HP}}$, $\Delta p_{3_{HP}}$) and LP ($\Delta p_{1_{LP}}$, $\Delta p_{2_{LP}}$, $\Delta p_{3_{LP}}$) flow pressure drops. The inlet pressure is p_{HP} while the outlet pressure is fixed at $1\,\mathrm{bar}$. The pressure difference across the JT-valve, Δp_{JT}, is depicted. To the right, a detail of the helium ph diagram shows that by increasing the pressure difference across the JT-valve, $\Delta p'_{JT} > \Delta p_{JT}$, the difference of enthalpies across the CIF is also increased, $\Delta h' > \Delta h$, respectively, and that the final temperature is lower.

The author of this report joined the project once CFHEX1 design had already been tested and CFHEX2 had been designed and manufactured. Therefore, the focus of the internship has been on the characterisation of CFHEX2.

The CFHEX design goals will necessarily drive the measurement campaign. Therefore, it is important to outline these briefly. The desired characteristics that the Cryolab aims to achieve for a concentric tube-in-tube design are:

- **High effectiveness**, meaning high heat transfer between the fluid streams, which in turn implies:

  - High heat transfer between the fluid and the CFHEX structure. This requires that the wetted area and the convective heat transfer coefficients to be high.
  - Low thermal conductivity in the axial flow direction of the CFHEX and high thermal conductivity in the direction perpendicular to the fluid flow in the CFHEX. This can be achieved by carefully selecting the materials and geometric configurations.

- **Minimum CFHEX pressure drop**. The LP outlet pressure (see Fig. 3.1) is limited to 1 bar in order to avoid going to lower-than-ambient pressure levels. This represents a limit for the lowest reachable pressure after the JT expansion. A big pressure difference Δp_{JT} across the JT-valve is desired because it implies that a higher enthalpy difference will be available for cooling in the two-phase region, as shown in the detail of Fig. 3.1. This can be summarised with the following equation, using the notation of Fig. 3.1 and neglecting transfer lines and cryocooler stage heat exchangers pressure drops:

$$\Delta p_{JT} = p_{HP} - (\Delta p_{1_{HP}} + \Delta p_{2_{HP}} + \Delta p_{3_{HP}}) - (1 + \Delta p_{1_{LP}} + \Delta p_{2_{LP}} + \Delta p_{3_{LP}}) \quad (3.1)$$

  Hence, the higher the CFHEXs pressure drop is, the lower the pressure difference across the JT-valve Δp_{JT} will be.

- **Uniform flow distribution** in the CFHEX passages.
- **Mechanical stability and leak tightness** of the CFHEX channels and outer shell.
- **Compactness and easy manufacturing** of the CFHEX.

In the next sections, the measurement process will be described. Before that, an introduction into the laboratory environment will be given. This includes a presentation of the set-up, as well as of the different materials and techniques used to perform measurements at very low temperatures.

3.2 Experimental environment

3.2.1 Laboratory set-up

The high level architecture of the measurement set-up is presented in Fig. 3.2. It is composed of four main systems: the remote cooling system, the data acquisition system, the control system and the support system.

The **remote cooling system** provides the cooling capability and allows running the experimental campaign for characterisation of the CFHEXs. It includes:

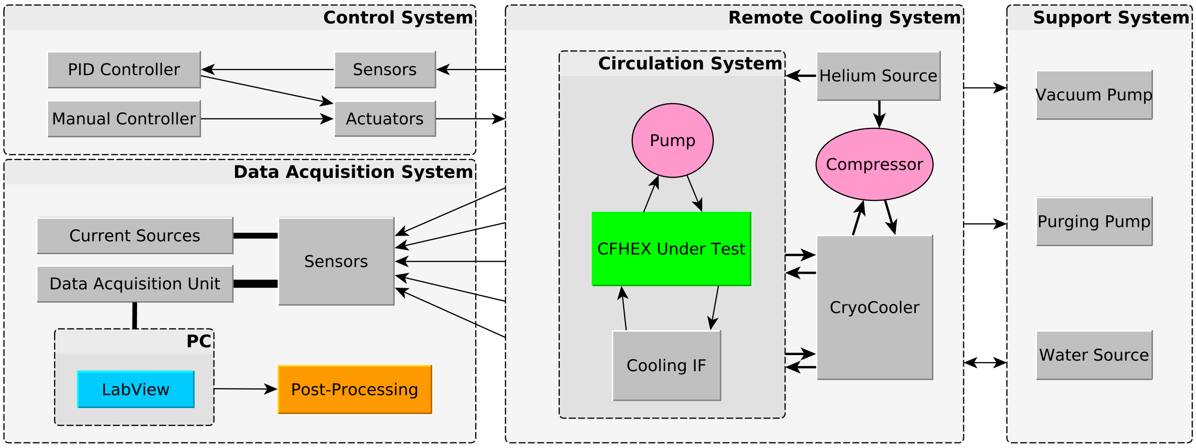

Figure 3.2: Architecture of the measurement set-up. It is comprised of a control system for controlling the sensors and actuators, a data acquisition system to collect the measured values, a remote cooling system containing the CFHEX to be tested, and a support system providing vacuum, purging and water sources.

- A novel CFHEX to be tested and characterised.
- A GM type cryocooler (model *Leybold RGD 1040*) with a water-cooled compressor (model *RW5*).
- A circulation system, which will provide transport of the cooling power to the CIF. It contains the novel CFHEX to be tested, a pump to circulate the fluid, and the CIF.

The **support system**, composed of a pump (see Fig. 3.10b), which evacuates the air and maintains the vacuum inside the chamber; a purging pump, which evacuates the helium circuit before use, and a water source, which provides cooling water for the crycooler compressor.

The **control system** manages the heaters mounted in different locations of the circulation system (actuators) with the purpose of imposing a specific behaviour. The system includes:

- A manual controller, *Hameg HM8143*, which can be used by the operator to provide a specific current to some of the the heaters.
- A proportional–integral–derivative (PID) *LakeShore 336 temperature controller*, which controls the current supplied to the heaters via a closed feedback loop with the temperature sensors used as the control input.

The PID controller ensures stable temperatures at the respctive locations for otherwise varying system parameters like mass flow rates or fluid parameters. This is particularly important when several tests are performed with different input conditions. In those cases, a constant temperature of certain parts of the set-up is often required. Furthermore, the manual controller is often utilised to simulate the heat loads in the CIF.

The **acquisition system** collects data from all the sensors so that the information can be stored and processed. It is composed of the following elements:

- A set of sensors, which measure temperature, pressure and mass flow rate.
- Several current sources, which supply the sensors with a constant current.
- A *Keithley 2700* multimeter, which measures all the voltages of the sensors and heaters. Based on these, the temperatures, pressures and the heater powers can be calculated using relevant dependencies.
- A PC with *LabView* installed and running, which collects the voltage data from the multimeter, process it, and store it for further analysis by the operator.

This configuration of the acquisition system provides an advantageous 4-wire measurement capability (see Fig. 3.3a). The current source provides a stable fixed value current which is independent of the resistance in the feeding wires. Moreover, the multimeter, that is, the voltage meter from Fig. 3.3a, measures directly on the legs of the sensor, excluding the current feeding wire resistance. The high internal resistance of the multimeter ensures that the current in the voltage measurement wires is negligible. Therefore, this combination makes the measurement very precise.

In contrast, a traditional simpler 2-wire measurement (See Fig. 3.3b) would be much less precise as the voltage is measured across both the sensor and the resistive wires. Typically, the resistance of the measurement cables ranges between $1\,\Omega$ and $20\,\Omega$. For a sensor resistance of typically under $100\,\Omega$, its measurement gets distorted significantly.

Due to its relevance, the circulation system, the sensors and the actuators will be addressed in more detail in the next sections.

3.2.2 Circulation system

The complete circulation system piping and instrumentation diagram is shown on Fig. 3.6. Its starting procedure consists in filling the system with helium-4 from the *GHe* bottle and purge with a vacuum pump to clean from impurities. The process is normally repeated three times. Once that is done, the circulation pump (P001) is turned on. More specifically, a *KNF N-143 ANE* pump is used. It will start to circulate the high-pressure helium in a clock-wise direction as shown in Fig. 3.6. Further helium flow pressurised by the pump passes through a water HEX where it gets re-cooled to room-temperature

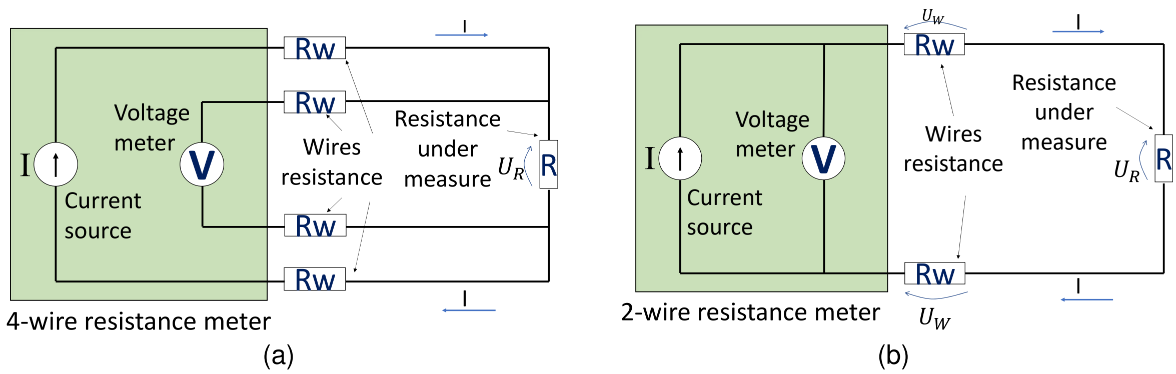

Figure 3.3: Sensor measurement techniques; (a) precise 4-wire measurement, where the voltage meter uses an independent wire, not affecting the feeding current; (b) less-precise 2-wire measurement, where both the feed and the measurement use the same wire. In this case, the measurement is being affected by the wire and interfaces resistance.

values. Next, it passes via a mass flow controller. The latter is the *F-004* valve and the *F-113AI* 3.4a thermal, bypass-type, mass flow meter from *Bronkhorst*. It consists of a thin capillary bypass tube that takes a percentage of an already imposed laminar flow. The bypass has two temperature sensors and a heater in between. Once the flow starts entering, the applied heat load creates a temperature gradient, as shown in Fig. 3.4b, that is proportional to the fluid's mass flow rate. The measurement is used as an input signal to the PID controller, which compares the measured mass flow rate to the desired one. Depending on the value, it will regulate the main valve.

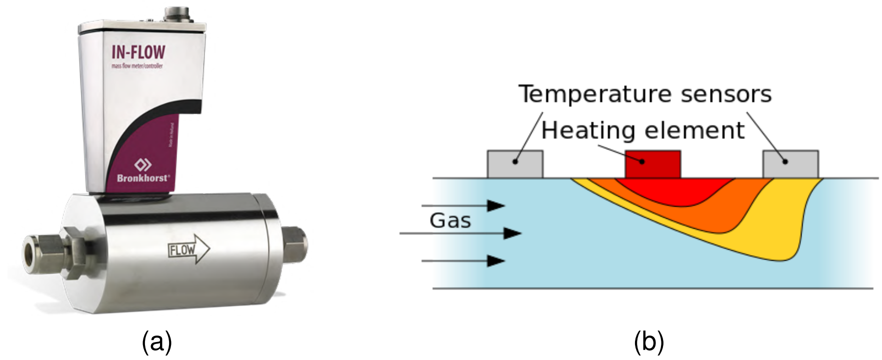

Figure 3.4: Mass flow controller used in the set-up; (a) shows a photograph of the actual valve and (b) depicts the principle by which it is capable of calculating the mass flow rate, i.e., by comparing the measured values of two temperature sensors with a heater physically placed in-between . Source: [15]

After the mass flow controller, helium enters the vacuum chamber with the desired mass flow rate. First, it passes through the first CFHEX, where it gets pre-cooled by the returning flow. It cools down further in the heat exchanger at the first stage of the cryocooler, passes through CFHEX2 and through the second stage HEX. Finally, the flow passes through the JT-valve, where it undergoes cool-down due to the isenthalpic expansion (see. Fig. 3.1) at a sufficiently low temperature. Next, the CIF is reached. The cold low pressure helium, absorbs the heat from the imposed heat load, and returns through CFHEXs 1 and 2, precooling the incoming warm high-pressure helium. As outlined previously, the good inlet pressure at the pump should be >1 bar.

There are several safety valves installed for the case where threshold pressure levels in the system are surpassed. Also, the system has two buffer volumes on LP and HP lines. The purpose of these is to absorb the vibrations coming from the pump. Finally, the *HV700* valve controls a small circuit that bypasses the rest of the elements. When it is fully open, no flow goes towards the mass flow controller.

Fig. 3.6 also depicts all the used sensors and heaters. Their location has been strategically chosen so that the tests can be performed within a single measurement campaign. In any case, sensor rearrangements are often needed to cover for a particular testing. Also, mechanical constraints of the set-up sometimes prevent the sensor from being located in its ideal position, e.g., the sensor TT210 had to be located under the top flange of CFHEX2 to measure its outlet LP stream temperature. Since this value is critical for the calculation of the effectiveness, a thermal analysis, shown in Fig. 3.5, was made to determine the heat transfer from the HP stream through the flow distributor, and account for it on the measured values by TT210.

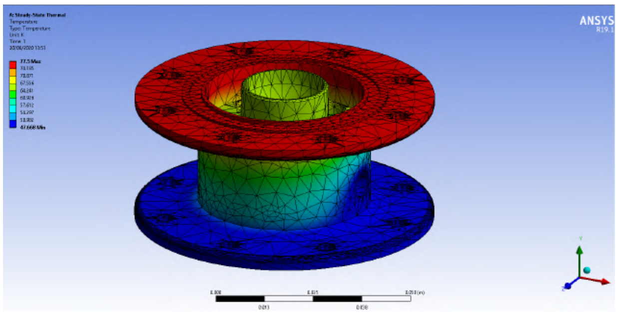

Figure 3.5: Flow distributor thermal simulation with ANSYS Mechanical 19. The temperature profile along the piece is depicted, where the warmest temperature is of 77.5 K at the top flange (in red), and the coldest is of 47.7 K at the bottom flange (in blue), recreating operational conditions.

The bypass valve, the helium bottle, the JT-valve, the heaters, and the mass flow controller are the control points of the circulation system. They enable the operator to set the desired pressure, temperature and mass flow conditions. They will be used for the different measurements that will be performed for the CFHEX2 characterisation.

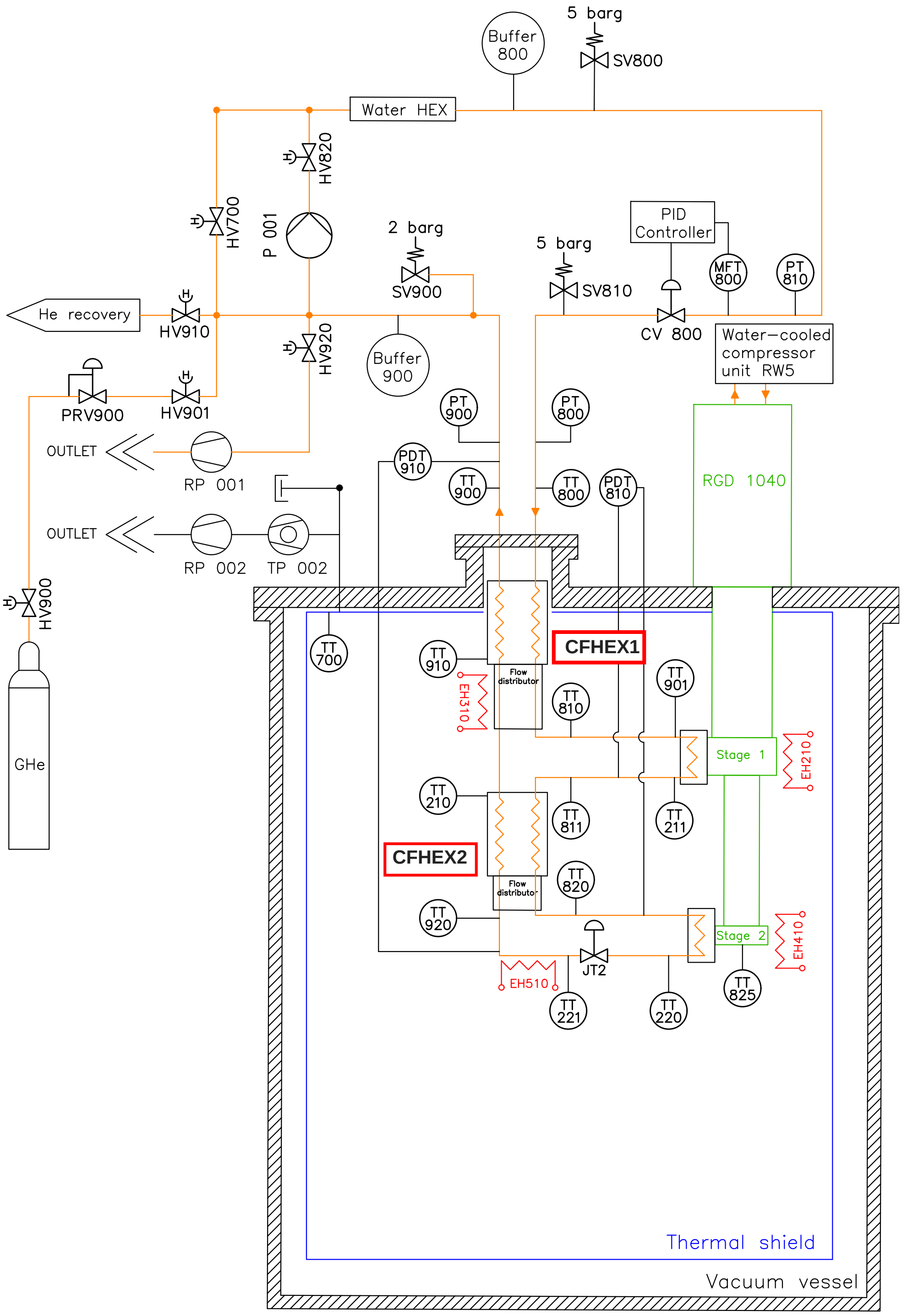

Figure 3.6: Set-up piping and instrumentation diagram (PID), depicting the convective loop with CFHEX1 and CFHEX2, the cryocooler, the used safety and hand valves, and the installed temperature (TTX) and pressure (PXX) sensors for a specific measurement campaign, among others. Courtesy: A. Onufrena.

3.2.3 Heaters

Heaters *EH210* and *EH410* together with sensors *TT211* and *TT825* are located on the first and second stage of the cryocooler, respectively, and are connected to the *LakeShore* PID Controller of the control system. Their main purpose is to maintain a stable temperature of the cryocooler stages.

The heater *EH310* is located on the flow distributor between CFHEX 1 and 2. It is of special importance during the measurement of the parasitic conduction heat loads on the system. This measurement campaign will be described in Sec. 3.3.3.

Finally, the heater *EH510* is located where the CIF would be, to simulate the heat loads on the system. Such test is useful to approximate the amount of the cooling power that is transported from the cryocooler to the CIF. More details on its procedure are given in Sec. 3.3.

All the heaters are made of a resistive structure on a polyimide (Kapton) film. This is an organic material that offers a flexible profile, very high dielectric capability and good resistance to radiation. Its flexibility allows wrapping the heaters around the pipes and ensuring good thermal contact.

3.2.4 Sensors

Three types of sensors can be found in the set-up. The pressure sensors, the temperature sensors and the mass flow rate meter. The latter has already been addressed. In the next paragraphs, pressure and temperature sensors will be described in more detail.

Pressure Sensors

There is an absolute pressure sensor (PT810) located before the mass flow rate controller, one at the system inlet (PT800), and one at the system outlet (PT900) of the vacuum chamber. These sensors measure the static pressure relative to vacuum. The first two are a *Rosemount 3051TA* while the last one is a *Keller series 33*. PT810 is needed to measure the maximum available pressure, PT800 to monitor the CFHEX1 inlet pressure, and PT900 to control the pressure levels going into the ciruclation pump at the outlet of the circulation loop.

Next, there are two relative pressure sensors, that measure the pressure difference between two locations in question. PDT810 measures the static pressure drop along CFHEX2, and PDT910 measures the low pressure side static pressure drop of both

CFHEXs together. These values are very relevant to the characterisation of the CFHEXs. Both sensors are *Rosemount*, model *3051CD*.

The functioning principle of differential pressure sensors is based on a flexible diaphragm movement. This diaphragm bends by a specific amount depending on the applied pressure. The sensor transforms this into an electrical signal, which is then interpreted by the data acquisition system.

Temperature Sensors

The temperature sensors are one of the most critical and sensitive parts of the data acquisition chain. Their values are of great importance for any subsequent conclusion about the CFHEX characterisation. Because of that, very precise and robust sensors are needed. Since parts of the system operate at low cryogenic temperatures, special and adapted sensors have to be used so that measurements data is precise.

The circulation system has a temperature gradient, with its warm end at the vacuum chamber input and its cold end at the CIF. Temperatures below $10\,\mathrm{K}$ are reached at the coldest locations. Special and expensive sensors need to be used there. On the warmer parts, a simpler and more common sensor is used instead. The following three types of temperature sensors were used depending on the temperature range of interest. They are depicted in Fig. 3.7.

- **Pt100**. It is the most common Resistance Temperature Detector (RTD) sensor. These sensors contain a resistor whose resistance changes linearly and proportionally to temperature. Physically, it consists in a coiled wire impregnated in a ceramic core or a thin deposited film. The change in resistance of the sensor with temperature is well documented and given as the sensor reference curves. During the measurement, a small current of $1\,\mathrm{mA}$ is fed into the sensor, and the resistance is then measured and translated into temperature using the reference curves. These sensors are widely used in laboratory environments. This makes them inexpensive and easily available. Nevertheless, their accuracy is good enough only above $80\,\mathrm{K}$. During the measurement, Pt100 sensors were also used for the locations at lower temperatures down to $\sim 45\,\mathrm{K}$. This was possible as they were thouroguhly callibrated against a more accurate TVO sensor for these ranges. Finally, an interesting advantage of these sensors is that they come in a variety of sizes, which can be very practical for some applications. Sensors TT800, TT900, TT810, TT910, TT901 and TT211 from Fig. 3.6 are Pt100.

- **CERNOX**. Specifically designed by *LakeShore Cryotronics Inc.* for monitoring superconducting magnets used in high energy accelerator facilities, these sensors offer great specifications for cryogenic temperatures below 20 K, e.g., good resolution, fast response and great stability with time. Specifically, their temperature measurement range is from 100 mK to 420 K. Since their resistance decreases when the temperature increases, they have a higher resolution at low temperatures. Calibrated CERNOX sensors can be costly. TT920 and TT820 from Fig. 3.6 are CERNOX.

- **TVO**. This is another type of a precise sensor for low temperatures. It behaves similarly to a CERNOX sensor, e.g., its resistance increases with decreasing temperature. However, TVO sensors are bigger in size, hence might not present the best solution if the temperature needs to be measured at a specific point. TT210, TT811, TT21 and TT220 from Fig. 3.6 are TVO.

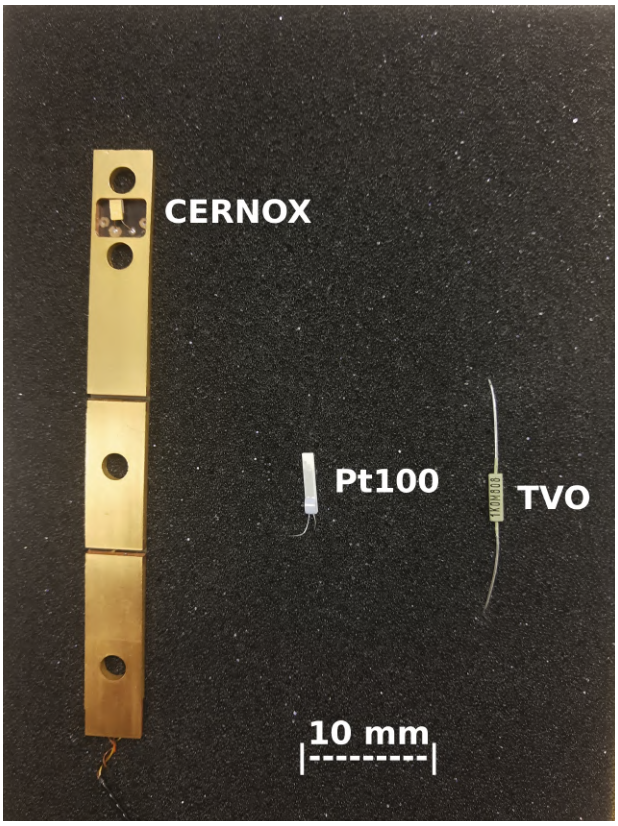

Figure 3.7: Picture of a CERNOX sensor with a thermalisation structure, Pt100 and TVO temperature sensors (from left to right).

3.2.5 Materials

The choice of materials used in the measurement set-up is critical to obtain the desired thermal and mechanical behaviour and enable the expected operation of the system. In this section, the choice of materials of the different parts of the system is described and justified.

The piping of the entire circulation system is made out of stainless steel. It can be seen in Fig. 3.8a, where the MLI has not been fully put yet. As described previously, stainless steel is a very common material in cryogenics, mainly because of its mechanical robustness. It has a poor thermal conductivity, especially at low temperatures, which helps to avoid thermal shortcuts. Finally, it offers a low out-gassing rate. The vacuum chamber, depicted in Fig. 3.9, is made out of stainless steel as well.

The radiation shield is made out of copper as good thermal conductivity is required to keep it uniformly cold and, hence reduce thermal radiation from the warmer surfaces towards the piping of the circulation loop.

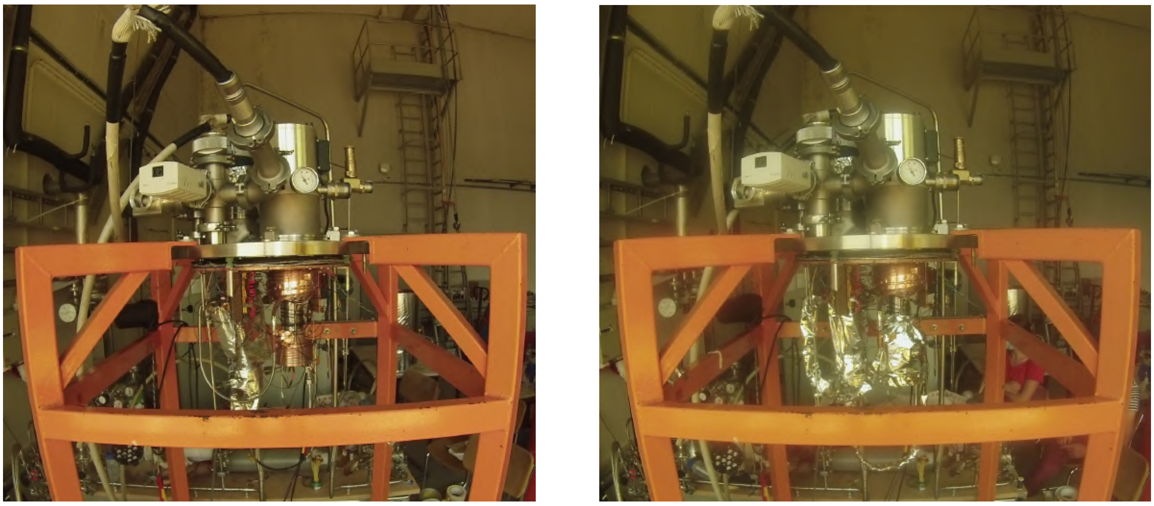

(a) (b)

Figure 3.8: MLI insulation; (a) picture of the opened set-up without MLI covering and (b) a picture of the set-up covered in MLI, ready to be closed.

Special materials are needed to properly attach the temperature sensors. First, isopropanol is used to clean the surface from impurities that can worsen the thermal contact between the temperature sensors and the surface. *Kapton* tape, which is a dielectric at low temperatures, is placed under the current leads of the sensor to protect them from electrically conducting surfaces, thus avoid shortenings. To improve thermal contact between the sensor and a surface, a high-thermal conductivity grease such as *Apiezon*

N is applied on the area. For further improvements, indium foil can be put around the sensor pad instead, since it is very soft and malleable and ensures a great contact between materials sealing. The sensor is pressed on the pipes using *teflon* tape. As the temperature decreases, the tape contracts ensuring a stronger mechanical contact between the surface and the sensor. On top of the *teflon*, a reflective tape is used to protect against incoming thermal radiation.

Finally, a MLI is put around the piping as shown in Fig. 3.8, leaving the system ready for the close-up, as depicted in 3.9. The added MLI seeks to reduce the incoming thermal radiation from the shield towards the lower temperature parts.

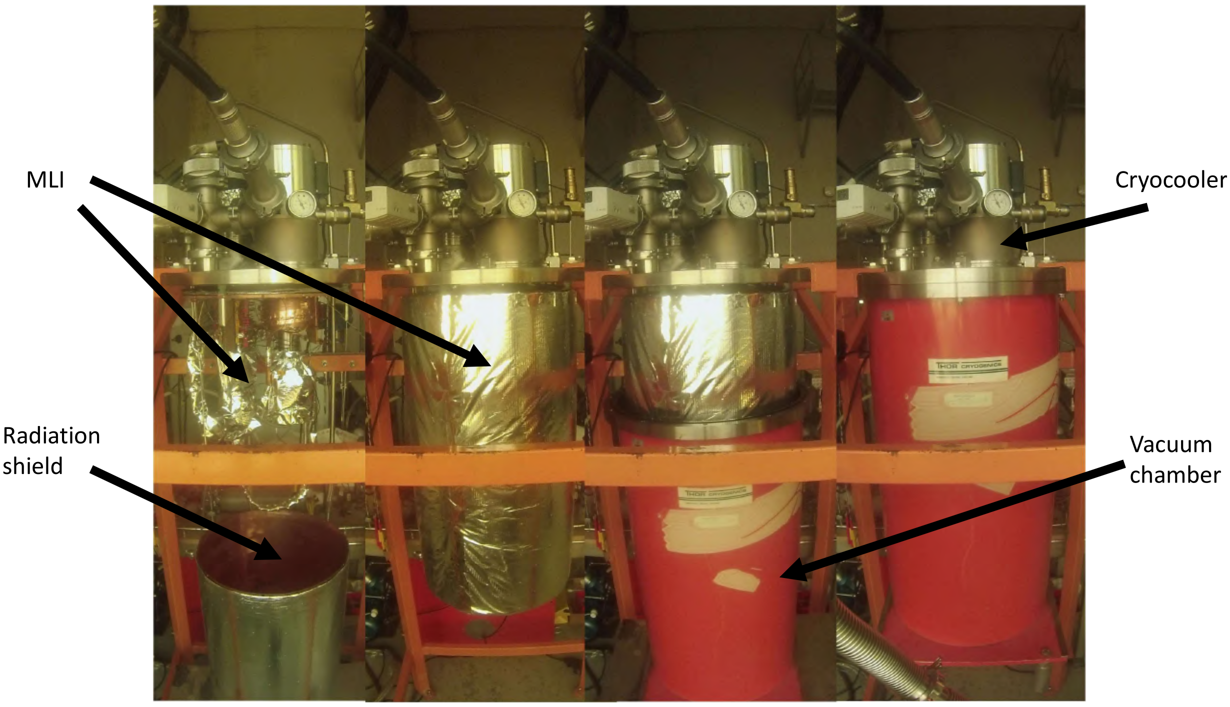

Figure 3.9: A series of photographs depicting the installation process of the set-up.

3.2.6 Cold measurement techniques

Significant errors can be incurred when working with experimental data since several uncertainties are combined. Even though individual error tends to be small, the combined uncertainty can quickly add up and grow. This can be illustrated with an example of the temperature measurement. A typical RTD sensor varies its electrical resistance when temperature changes. To measure the resistance, voltage is measured, while the used current and its accuracy are known. The voltage measurement has noise implicit in its values. Precision error from the measuring multimeter is added. When calculating the resistance, respective accuracies of voltage and current measurement are combined. Finally, resistance is transformed into temperature using a fit to tabulated calibration values provided by the manufacturer. Hence, a fitting error is also added into the final accuracy. The contributions of all these error sources must be taken into account. A sample of these is shown in Tab. 3.1 for a measurement with each of the sensors of the set-up. The resultant errors will also be depicted in Fig. 3.11-3.15 to give the reader a notion of the measurement uncertainty.

Equipment	Uncertainty
Pt100	0.1 K at 295 K, 0.56 K at 80 K
CERNOX	0.15 K at 10 K, 0.18 K at 50 K
TVO	0.16 K at 10 K, 0.28 K at 50 K
PDT810 and **PDT910**	0.16 mbar and 0.42 mbar
PT800 and **PT900**	14 mbar and 12 mbar
Mass flow controller	max. $2.75\,\mathrm{mg\,s^{-1}}$ for $250\,\mathrm{mg\,s^{-1}}$ of He

Table 3.1: Sample uncertainties of the laboratory set-up for a measurement with each of the available sensors at typical test conditions.

When doing high-precision measurements, the focus is always on reduction of the measurement errors. Calibration is a useful technique to reduce the total measurement error.

For the set-up, TVOs and CERNOXes are calibrated by the manufacturer. Pt100 sensors are using a standard curve based on ITS90. However, the acquisition chain can introduce errors in the measurement. Therefore, it has been decided that a calibration at cold and warm has to be performed for the Pt100 so that the error source from the acquisition chain and the sensor variation is accounted in new calibration curves. For the calibration at warmer temperatures, a pot full of distilled water with ice at 0 °C saturation conditions was used. All the Pt100 were submerged into this water while their resistance was being recorded. This gave an offset relative to each's sensor default curve, which was then used to create the new calibrated curve that accounted for the acquisition chain errors. For low temperature measurements using Pt100 sensors, these were calibrated against a more accurate TVO reference sensor. In this case, uncertainty of the TVO will be added to the uncertainty of the Pt100 sensors.

To accomplish the temperature measurements,the sensor cables need to be thermalised to reduce heat transfer by conduction. This means the sensor electrical cables were thermally anchored at the thermal shield temperature level and at each of the sensor locations. For this, thermalisation pads are used as shown in Fig. 3.10a. Those consist on a refrigerated connector that joins a warm end of the electrical line with the sensor end. The connector has to be as close as possible of the respective sensor.

Finally, a 4-wire measurement, as depicted in Fig. 3.3a, is used for the Data Acquisition System. This technique ensures better precision since it avoids measuring the resistance of the current wires as explained in Sec. 3.2.1. The material of the current cables of the sensors is selected so that optimum between low thermal conduction and resistive self-heating is reached. The best candidate that complies with such requirement is manganin, which is a copper-manganese-nickel alloy. In contrast, for the heater current cables, where higher currents are used, copper is the chosen material as good electrical conductivity is necessary.

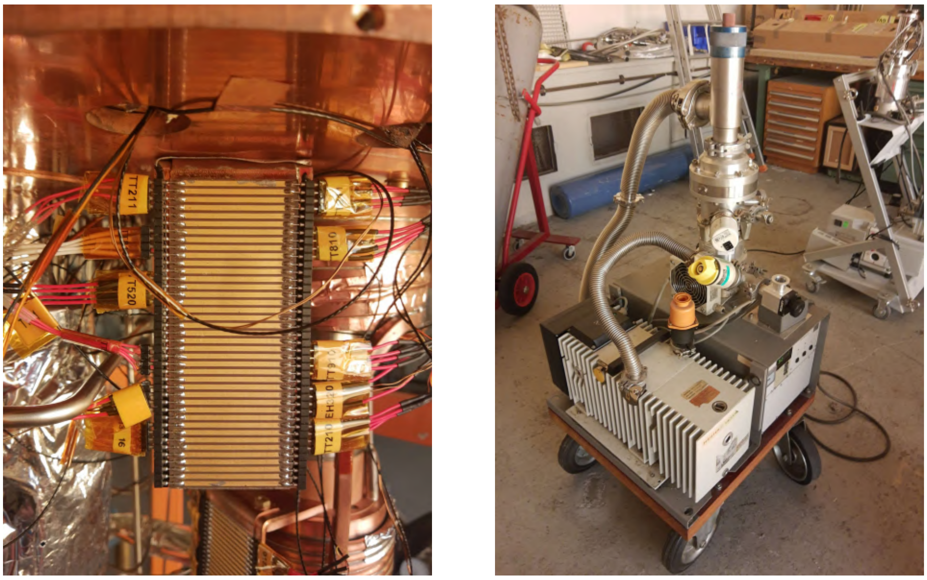

(a) (b)

Figure 3.10: Parts of the set-up equipment; (a) thermalisation pad used to thermalise cables connecting a warm end with a cold end, reducing the heat transfer by conduction and (b) turbopump and roughing pump used to extract air from the vacuum chamber providing an insulation vacuum of at least 10^{-6} bar.

3.3 Test campaigns

Three test campaigns were performed during the duration of the internship. Within each campaign, different types of measurements were conducted.

3.3.1 Starting a campaign

In order to start a campaign the system has to be closed first. This means putting on the radiation shield with its MLI wrapping and the vacuum chamber. This process is illustrated in Fig. 3.9.

Once the thermal shield and vacuum chamber are attached to the top flange of the set-up, vacuum is progressively created inside the vacuum chamber. This is done with a vacuum pump system that is composed, for this set-up, of a turbopump plus a roughing/backing pump (see Fig. 3.10b). The latter will create vacuum in the order of 10^{-2} mbar and then the turbopump will start operating, creating vacuum levels up to 10^{-7} mbar. This will take about a day for this specific set-up. It is necessary to perform this action before starting the cool down because otherwise, impurities would be solidified on the cryogenic surfaces.

Once vacuum is ensured inside the chamber, the circulation system is started. The water has to be opened first for the cryocooler compressor and for the first precooling HEX, denoted 'Water HEX' in Fig. 3.6. Next, a purge is done three times with helium in order to clean the system from impurities inside the pipes. The venting is done with a specific dry (oil-free) pump to avoid the risk of oil contamination. Helium is then put into the loop from the supply, the circulation pump is started, and the cryocooler is turned on. After a while, the temperatures in the system will have stabilised everywhere in the circulation loop, and the set-up will be ready to start the measurement. This cool-down process normally takes 24 h for stabilisation of the temperature and pressure conditions.

3.3.2 Ending a campaign

Once the desired measurements have been performed, it is time to open the system. It may be the end of all the test campaigns or some modifications may have to be introduced before starting a new campaign.

The process to end the campaign is almost the inverse from the starting one. First, the cryocooler is turned off, such that the system begins to warm up. The water circulation is switched off as well. The circulation of the helium gas helps speeding up the warming-up process, which takes approximately 24 h. Ideally, the circulation loop should be at 1.5 bar for the high-pressure line and 1 bar for the low pressure. This will ease the functioning of the ciruclation pump, while avoiding any leaks into the system.

With the system being above $\sim$285 K, the circulation pump can be switched off. Next, the vacuum chamber can be repressurised by turning off the vacuum pumps and slowly filling it with air. The vacuum pumps have to be switched off in a specific way. The roughing pump has to be turned off first, and the valve towards the turbopump has to be immediately closed. Otherwise, there is a risk of oil from the roughing pump contaminating the system. After this is done, the thermal shield and the vacuum chamber can be dismounted. The system is now open and modifications can be done if needed.

3.3.3 Measurements

The focus of the project has been the characterisation of CFHEX2. Aleksandra Onufrena had already performed the characterisation tests on CFHEX1. Thanks to that experience, most of the desired measurements that had to be performed where clearly defined. In general terms, the idea is to determine the performance of the heat exchanger at different operating conditions. From there, the results are to be compared to the heat exchanger model, seeking to understand the physics behind, and to improve the model if possible. Finally, an operating range for different applications can be determined for the heat exchanger in order to ensure the optimum performance.

Pressure, mass flow rate and temperature are the main parameters that can influence the performance of the exchanger. Therefore, the tests seek to see how alterations on each of those contribute into the overall behaviour of the CFHEX. The testing approach for this has been to fix two parameters, while varying the third.

The parameters that define the performance are the effectiveness, as defined in Sec. 2.3, and the pressure drop in both the low-pressure and the high-pressure CFHEXs streams. Therefore, these are the variables that will be followed closely when modifying the different parameters. High effectiveness and low pressure drop are desired.

Following this reasoning, two tests were performed:

- **Pressure variation measurement**: inlet pressure is varied, while mass flow rate and temperature are maintained constant.
- **Mass flow rate variation measurement**: mass flow rate is varied while the pressure and temperature conditions are kept constant.

The control range for the temperature of the CFHEX HP and LP inlet flows is very limited. With the current set-up, it is only possible to keep it relatively constant with the help of several heaters. However, unlike with $\dot{m}$ and p measurements, a wide range of CFHEX inlet temperatures can not be performed. The only way to create a set of different operating temperatures for further analysis is to redirect the piping to bypass the first stage HEX. This would allow to bring the CFHEX end temperatures from 12 K-50 K to 50 K-290 K.

Lastly, it is also important to see how the heat exchanger behaves within the entire remote cooling system. The following measurements were performed with that purpose in mind.

- **Static loads measurement**: the circulation loop is purged completely to thermally decouple the CFHEX from the cryocooler, and a heater is used to accelerate its warming up. By measuring the warm-up times for different heating powers, it is possible to obtain the parasitic heat load that is incoming from the exterior of the set-up by conduction. The objective is to determine the heat load by conduction through CFHEX2. The value for CFHEX1 has been already measured. The measurement is using a technique described further in the section. Unknown and complex interfaces between elements makes an analytical calculation very complex.

- **Transported power measurement**: measures the amount of cooling power that can be produced at the CIF and compares it to the amount of power available at the cryocooler second stage. This measurement allows comparing the performance of the remote cooling system to that of the cryocooler alone. The measurement is done once again with the help of two heaters. Several heat loads are delivered into the CIF and the temperature is recorded. Next, the same temperature levels are achieved directly at the second stage of the cryocooler with a second heater. The powers required to reach the temperature by the second heater are then compared to the imposed powers at the CIF. This gives the transported power ratio, which is an important parameter for the system performance characterisation.

Results Analysis

The error bars in the figures of this section represent the uncertainties of each measurement as presented in Sec. 3.2.6. Only vertical error bars are plotted since the uncertainty of the independent variables is within the size of the points.

The pressure variation measurements are depicted in Fig. 3.11-3.12. Fig. 3.11 shows the inlet pressure (p_{in}) effect on the pressure drop along the CFHEX HP stream (Δp_{HP}). These two variables are inversely proportional, i.e., for higher p_{in}, Δp_{HP} reduces. The figure also shows the directly proportional relation of the mass flow rate $\dot{m}$ on Δp_{HP}. This effect will be analysed further later on. Fig. 3.12 relates the effectiveness, ϵ, with p_{in} and $\dot{m}$. Again, higher mass flow rates are required to read the highest effectiveness. However, in this case the input pressure is almost not influencing the effectiveness. From these results it is clear that the CFHEX should ideally be operated at a high pressure and a high mass flow rate. Nevertheless, lower inlet pressure levels could be accepted too, since the pressure drop has shown to be relatively low, and hence not critical for our application.

The mass flow rate variation measurements are shown in Fig. 3.13-3.14 . The three test runs offer very similar values. Test 1 operated CFHEX2 at lower temperatures and inlet pressures (47 K-10 K and 2.1 bar) than test 2 and 3, which operated it in slightly different conditions (57.5 K-12 K and 2.3 bar). The effect on the pressure drop along the HP stream of the CFHEX with respect to the mass flow rate is depicted in Fig. 3.13, showing a clear correlation between the two. The pressure drop increases for higher mass flow rates. It can be seen that for the higher range of mass flow rates, there is a variance on the pressure drop along the HP fluid stream, of up to 1 mbar which is not included in the error bars. Such variation is acceptable for this application but should be further investigated if these pressure drop levels become relevant. Effectiveness variation with $\dot{m}$ on the other hand, depicted in Fig. 3.14, while quite constant, presents an optimum of 98 % at 150 mg s^{-1}. This is a very high value, fulfilling the objectives for which the CFHEX was designed. The system operating mass flow rate choice of point should mainly focus on the effectiveness as the pressure drop values are very low.

Finally, Fig. 3.15 represents the variation of the heating power with the inverse time t, where t represents the time that the set-up takes to reach a specific temperature indicated in the legend of the graph. This data allows the parasitic load to be computed. It can be calculated by finding the point where all the temperature curves cross the y-axis. This is demonstrated by the following reasoning:

$$\dot{Q}_{stat} = mc_p\frac{\Delta T}{\tau} \tag{3.2}$$

Where $\dot{Q}_{stat}$ represents the static load, m is the mass of the set-up, c_p, its heat capacity, ΔT is the temperature difference between the top and bottom flow distributors and τ is the time the bottom flow distributor takes to reach a set temperature. If the power of the heater, P, at the second flow distributor is added to the equation:

$$\dot{Q}_{stat} + P = mc_p\frac{\Delta T}{\tau} \tag{3.3}$$

From this, it can be concluded that:

$$1/\tau \to 0 \implies P \to -\dot{Q}_{stat} \tag{3.4}$$

Therefore, when $1/\tau \to 0$, that is, at the intersection point of the curves with the y-axis, the value of P has been found to be -0.24 W and hence, $\dot{Q}_{stat}$ is 0.24 W. However, maintaining constant the temperature at the top of CFHEX2 has been challenging since the system would warm up by itself very quickly. This led to short heating times, which added to the low parasitic heat loads at CFHEX2, made the measurement less accurate. In any case, the found value of 0.24 K supports the chosen design of CFHEX2, with very low axial thermal conductivities that enable the high effectiveness.

Finally, the transported power measurement test was performed concluding that, with two CFHEXs, 60 % of the power is being transported to the CIF. This value is expected to be improved once the third CFHEX is installed as the JT-valve will still provide cooling effect.

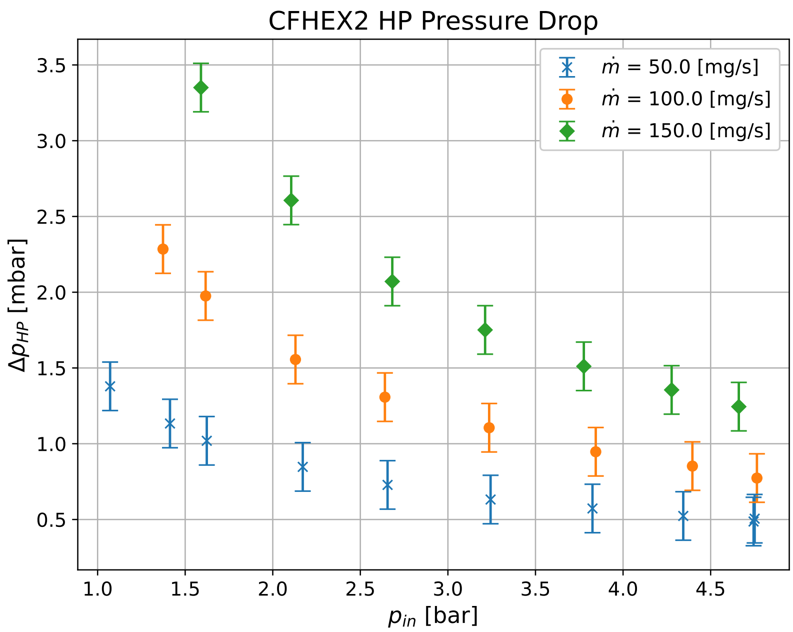

Figure 3.11: Pressure variation measurement 1. Pressure drop along the CFHEX2 HP stream (Δp_{HP}) variation with the inlet pressure (p_{in}) and the mass flow rate ($\dot{m}$).

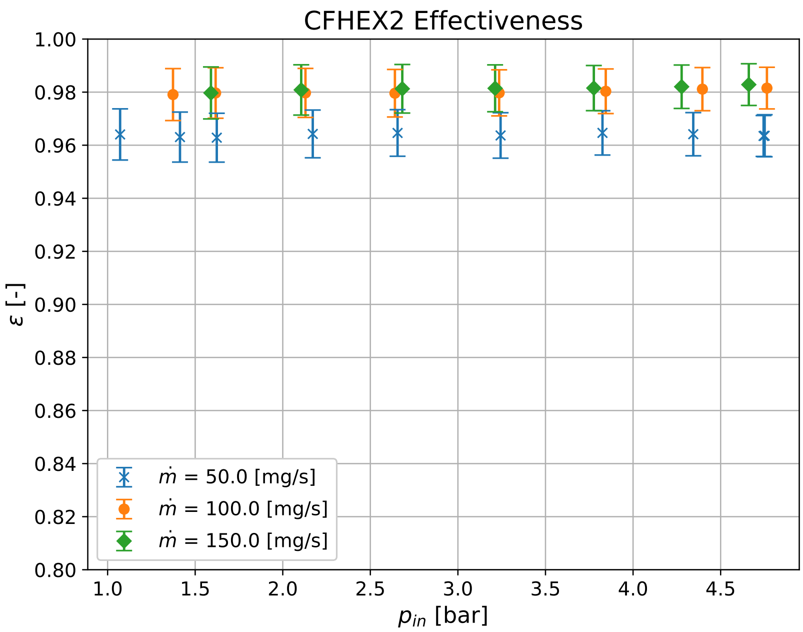

Figure 3.12: Pressure variation measurement 2. CFHEX2 effectiveness (ϵ) variation with the inlet pressure (p_{in}) and the mass flow rate ($\dot{m}$).

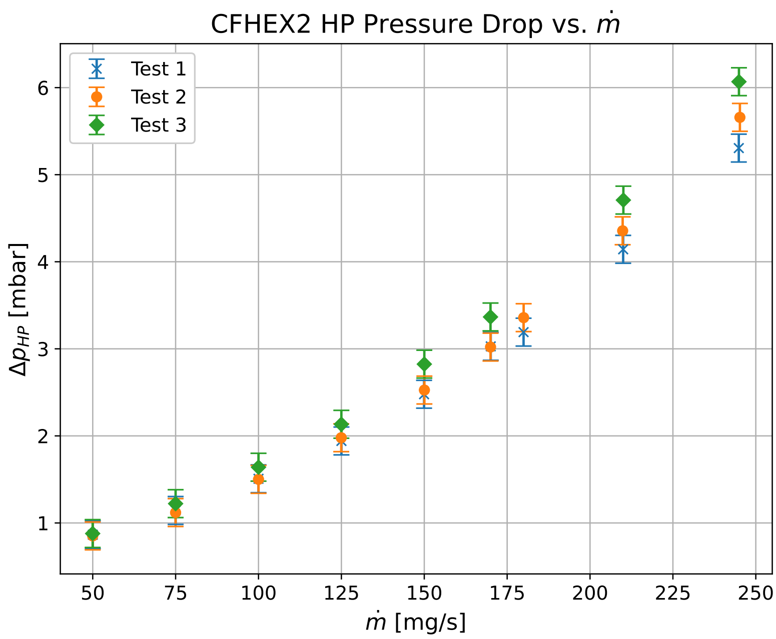

Figure 3.13: Mass flow variation measurements 1, showing the influence of the mass flow rate ($\dot{m}$) on Δp_{HP}.

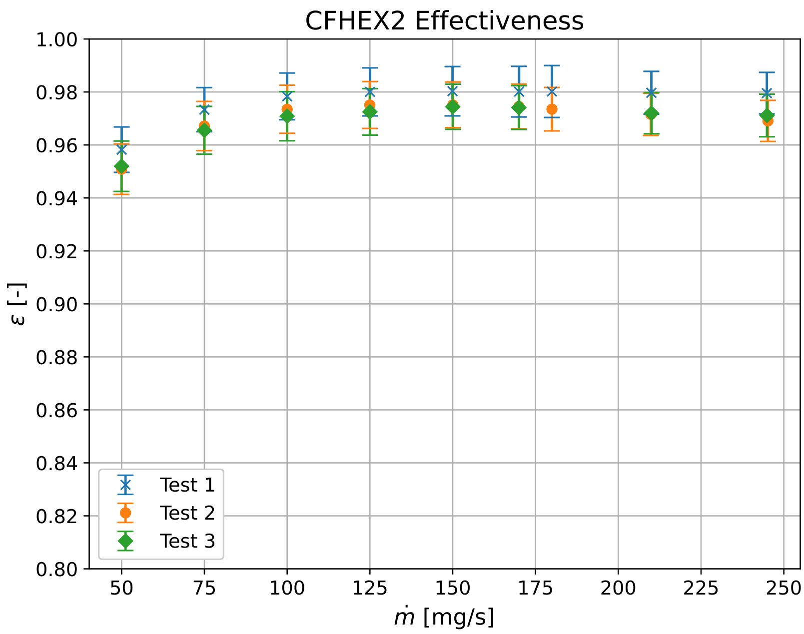

Figure 3.14: Mass flow variation measurements 2, showing the influence of the mass flow rate ($\dot{m}$) on the effectiveness (ϵ) of the CFHEX.

3.3.4 Results post-processing

Post-processing of the raw data coming from the sensors is a critical part of the analysis. It has to be done continuously, so that problems can be detected early on. Sensor voltages are transformed into temperatures and pressures by a LabView program. However, this data is still to be filtered so that only the relevant data regions are retained. The filtering part was done with a Python script, which selects and averages the stable data regions. From there, the post-processed measurement points can be combined into useful plots such as those presented in the previous section. The entire chain is depicted in Fig. 3.16.

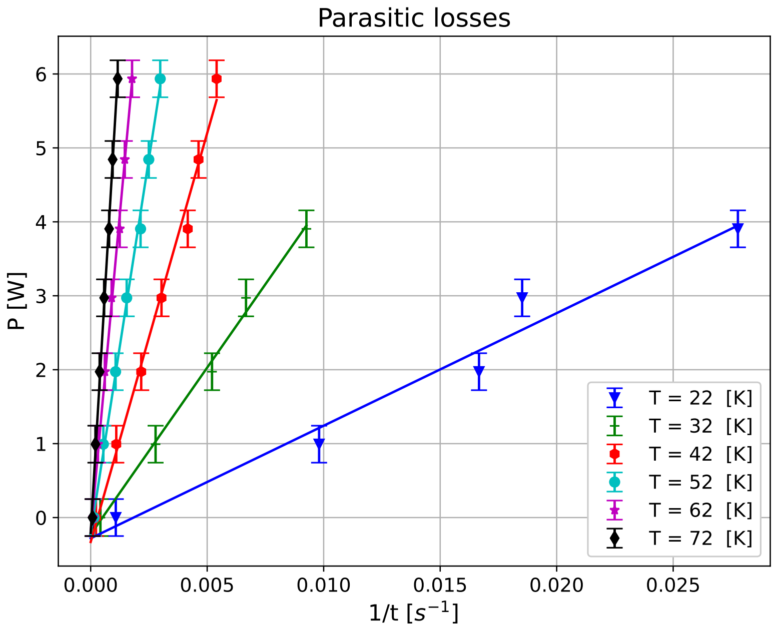

Figure 3.15: Parasitic CFHEX2 loads. Heating powers P at the bottom of the CFHEX2 versus the inverse time 1/t, where t is the time taken for the bottom of the CFHEX to read the temperature indicated in the legend.

Sometimes, physical limitations of the measurements have to be accounted for in the analysis scripts. This can cause the code to become more complex. The calculation of the pressure drop along the low pressure side of CFHEX2 (Δp_{LP}) is a good example to illustrate this. For the three test campaigns described above, the LP stream of the circulation system was equipped with an absolute pressure sensor at the output of the system (PT900) and a differential one (PDT910) between the input of the LP stream of CFHEX2 and the output of the LP stream of CFHEX1, see Fig. 3.6. Therefore, to compute Δp_{LP}, the pressure drop along the LP stream of CFHEX1 is needed. For that,

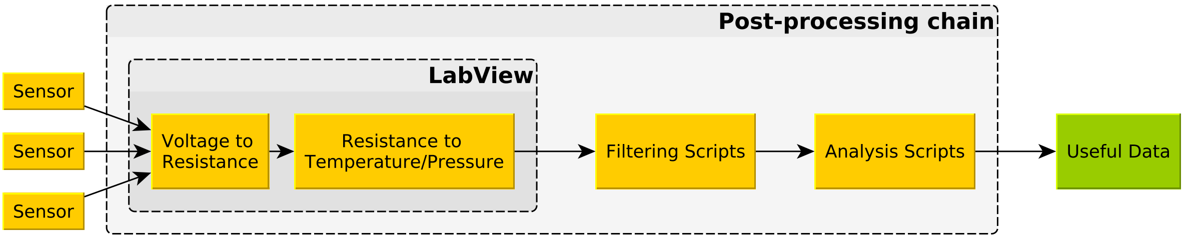

Figure 3.16: Post-processing chain for transforming raw data into useful data, with the help of a LabView program, a filtering script, and an analysis script.

the latter will be subtracted from the differential pressure drop between the two heat exchangers measured by PDT910.

In order to do that, an interpolation function for the CFHEX1 LP stream pressure drop data had to be programmed. This proved to be a complex task since it was a four-dimension function where the pressure drop depends on the temperature, mass flow rate and output pressure. Hence, machine-learning was deemed to be the fastest approach. The measurement data was used to train a Python library (Sklearn) linear regression model. The obtained model could then be used to predict the pressure drop across CFHEX1 LP stream for any combination of temperature, mass flow rate and output pressure. This would then be used to find the Δp_{LP}. The results of this process are shown in Fig. 3.17, where Δp_{LP} is plotted versus the outlet pressure for two different mass flow rates. The plot shows that the behaviour is similar to the one obtained for the HP stream (see Fig. 3.11), that is, the pressure drop slightly decreases with the outlet pressure for both mass flow values. It is interesting to note that the order of magnitude of the pressure drop is very small here. On the other hand, the error bars are quite significant here due to the calculation method.

3.4 Numerical model of a concentric CFHEX without a mesh

Both CFHEX 1 and 2 are based on a concentric tube design that uses a mesh to improve its transverse heat transfer. The CFHEX performance optimisation focus so far has been mainly on the inner wall material and interface between the mesh and the inner tube. However, it is also interesting to evaluate the contribution of the mesh itself on the effectiveness. With that purpose in mind, a simpler concentric counterflow heat exchanger with no mesh, schematically shown in Fig. 3.18, has been numerically modelled and analysed. Its predicted effectiveness will be compared with the meshed

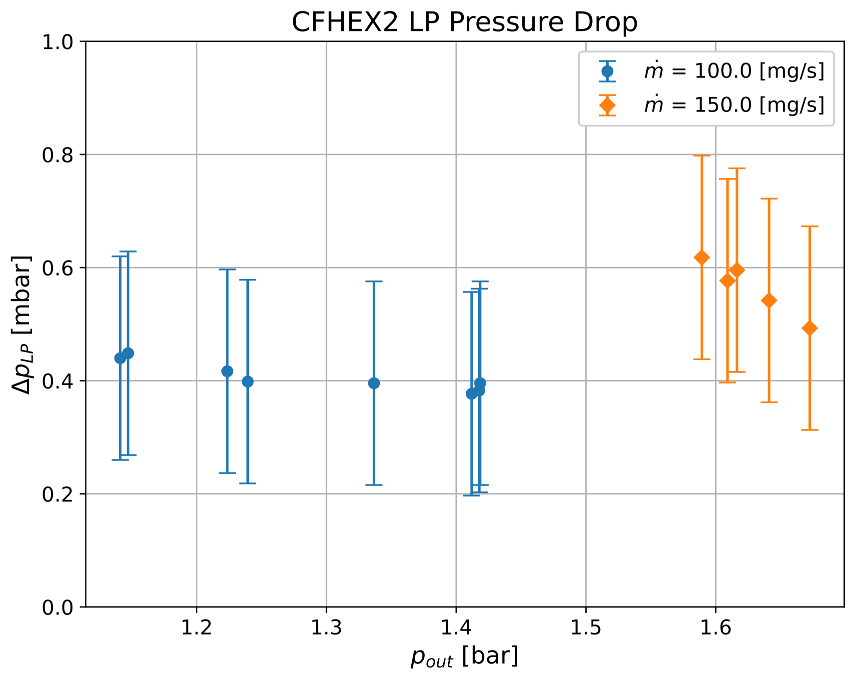

Figure 3.17: Pressure drop along the LP side of CFHEX2 versus the outlet pressure of the circulation loop, for two different mass flow rates.

version.

A Finite Volume Method (FVM) has been used for the discretisation of the CFHEX. Node-centered cells have been used for the solid walls, and cell-centered ones for the inner and outer flows.

For the cell-centered cells, the conservation of mass, linear momentum and energy equations have been applied. That is, respectively:

$$\frac{\partial}{\partial t}\int_{C.V.}\rho dv+\int_{C.S.}\rho\vec{v}\vec{n}dS=0 \tag{3.5}$$

$$\frac{\partial}{\partial t}\int_{C.V.}\vec{v}\rho dv+\int_{C.S.}\vec{v}\rho\vec{v}\vec{n}dS=-\int_{C.S.}p\vec{n}dS+\int_{C.S.}\vec{n}\vec{\tau}dS+\int_{C.V.}g\rho dV \tag{3.6}$$

$$\frac{\partial}{\partial t}\int_{C.V.}(h+e_c+e_p)\rho dv+\int_{C.S.}(h+e_c+e_p)\rho\vec{v}\vec{n}dS=-\int_{C.S.}\vec{q}\vec{n}dS+\int_{C.S.}\vec{v}\vec{f_{surf}}dS \tag{3.7}$$

Where S represents the surface, v the volume, ρ the density, g the gravity, h the enthalpy, e_c the kinetic energy, e_p the potential energy and where $\vec{n}$ is the normal surface vector, $\vec{v}$ the velocity, $\vec{\tau}$ the stress, $\vec{q}$ the heat flux and $\vec{f_{surf}}$ the surface forces.

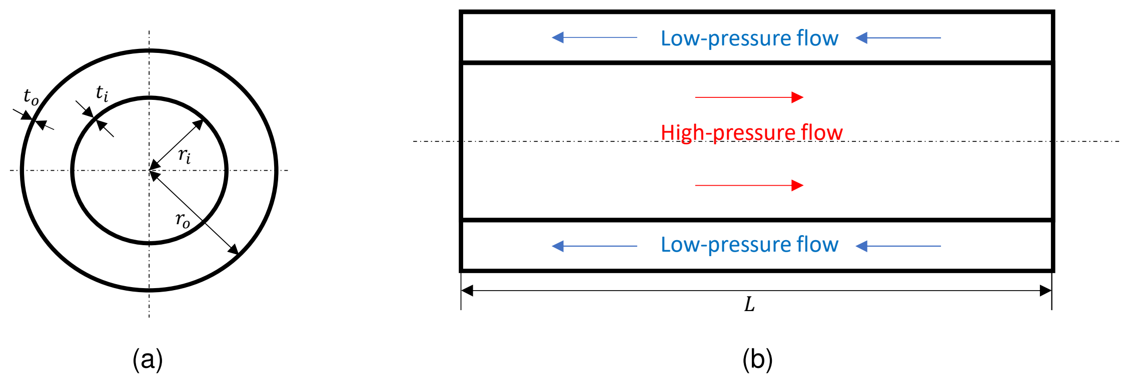

Figure 3.18: View of the concentric pipe heat exchanger; (a) frontal view and (b) lateral view

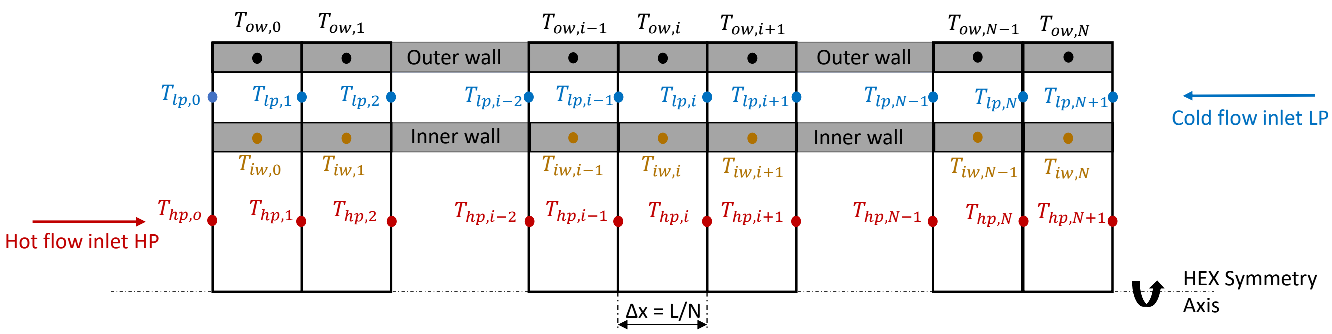

Figure 3.19: CFHEX no mesh model discretisation profiting from axial symmetry. The hot high-pressure (hp) flow is passing through the inner pipe from left to right, while the cold low-pressure flow (lp) is passing through the outer pipe from right to left. The inner wall (iw) serves as an interface between the two stream and the outer wall (ow) ideally avoids other heat loads from warming the lp flow. Wall edges, inner, and outer pipe outlet nodes are considered adiabatic for the analysis. The length of each cell (Δx) is the ratio between the total length of the tubes (L), and the number of volumes (N) used in the numerical model.

The following simplifications have been applied:

- Steady-state analysis $\Longrightarrow \frac{\partial}{\partial t} = 0$.
- Body forces are neglected since the differences in height of the studied heat-exchanger are very low $\Longrightarrow \int_{C.V.} g\rho dV = 0$.
- Surface force work is negligible relatively to the heat flux $\Longrightarrow \int_{C.S.} \vec{v} \vec{f_{surf}} dS = 0$.

- The difference of kinetic or potential energy is very small compared to the heat flux $\Longrightarrow \Delta e_c \approx 0$ and $\Delta e_p \approx 0$.

Yielding:

$$\int_{C.S.} \rho \vec{v} \vec{n} dS = 0 \tag{3.8}$$

$$\int_{C.S.} \vec{v} \rho \vec{v} \vec{n} dS = -\int_{C.S.} p \vec{n} dS + \int_{C.S.} \vec{n} \vec{\tau} dS \tag{3.9}$$

$$\int_{C.S.} h \rho \vec{v} \vec{n} dS = -\int_{C.S.} \vec{q} \vec{n} dS \tag{3.10}$$

The next step consists in transforming these equations into numerically discretised form.

Notation

Fig. 3.18-3.19 set the basis for the notation of the following equations. For the flow streams, some properties are calculated per node and some other per cell. To reduce notation overhead, the index (i') is used. The flow cell notation is defined in the same way as the solid wall nodes. Therefore, $\alpha_{lp\_ow,i'}$, for example, is the heat transfer coefficient between the low pressure flow with the outer wall at cell i', which is located between nodes i and $i+1$. Furthermore, Reyndols, Prandtl and Nusselt numbers are referred to as Re, Pr and Nu, respectively. Lastly, a line over a variable implies that it is the average value in a cell i', between nodes i and $i+1$, e.g., $\overline{\rho_{hp,i'}}$ is the same as $\frac{\rho_{hp,i}+\rho_{hp,i+1}}{2}$.

Hence, for the inner flow (hp):

$$\dot{m}_{hp,i+1} = \dot{m}_{in} = \rho_{hp,i+1} u_{hp,i+1} S_{hp} \tag{3.11}$$

$$\dot{m}_{hp}(u_{hp,i+1} - u_{hp,i}) = p_{hp,i} S_{hp} - p_{hp,i+1} S_{hp} - f_{iw\_in,i'} \overline{\rho_{hp,i'}} \frac{\overline{u_{hp,i'}}^2}{2} S_{iw\_in\_dx} \tag{3.12}$$

$$\dot{m}_{hp} C_{p_{hp,i'}} (T_{hp,i+1} - T_{hp,i}) = \alpha_{hp,i'} (T_{iw,i'} - \overline{T_{hp,i'}}) S_{iw\_in\_dx} \tag{3.13}$$

Where:

- $S_{hp} = \pi r_i^2$ gives the area of the inner pipe,
- $S_{iw\_in\_dx} = 2\pi r_i \Delta x$, gives the wet area of the inner surface of the inner wall,
- $C_{p_{hp,i'}}$ is the heat capacity of cell i' at its averaged temperature $\overline{T_{hp,i'}} = \frac{T_{hp,i}+T_{hp,i+1}}{2}$,

- The convective heat transfer coefficient $\alpha_{hp,i'}$ and the friction factor $f_{iw\_in,i'}$ are calculated following the tables [8], after obtaining Re, Pr and Nu from the average cell i' temperature and pressure.

For the outer flow (lp), the flow is going into the opposite direction. Therefore, the equations are solved starting from the last node:

$$\dot{m}_{lp,i} = \dot{m}_{in} = \rho_{lp,i} u_{lp,i} S_{lp} \tag{3.14}$$

$$\begin{aligned}\dot{m}_{lp}(u_{lp,i} - u_{lp,i+1}) = p_{lp,i+1} S_{lp} - p_{lp,i} S_{lp} - \overline{\rho_{lp,i'}} \frac{\overline{u_{lp,i'}}^2}{2} f_{iw\_out,i'} S_{iw\_out\_dx} \\ - \overline{\rho_{lp,i'}} \frac{\overline{u_{lp,i'}}^2}{2} f_{ow\_in,i'} S_{ow\_in\_dx}\end{aligned} \tag{3.15}$$

$$\begin{aligned}\dot{m}_{lp} C_{p_{lp,i'}} (T_{lp,i} - T_{lp,i+1}) = \alpha_{lp\_iw,i'} (T_{iw,i'} - \overline{T_{lp,i'}}) S_{iw\_out\_dx} + \\ \alpha_{lp\_ow,i'} (T_{ow,i'} - \overline{T_{lp,i'}}) S_{ow\_in\_dx}\end{aligned} \tag{3.16}$$

Where:

- $S_{lp} = \pi(r_o^2 - (r_i + t_i)^2)$ gives the area of the outer pipe,
- $S_{iw\_out\_dx} = 2\pi(r_i + t_i)\Delta x$ gives the wet area of the outer surface of the inner wall,
- $S_{ow\_in\_dx} = 2\pi r_o \Delta x$ gives the wet area of the inner surface of the outer wall,
- $C_{p_{lp,i'}}$ is the heat capacity of the fluid cell i' at its averaged temperature $\overline{T_{lp,i'}} = \frac{T_{lp,i}+T_{lp,i+1}}{2}$.
- $\alpha_{lp\_ow,i'}, \alpha_{lp\_iw,i'}, f_{ow\_in,i'}$ and $f_{iw\_out,i}$ are calculated following the tables [8], after obtaining Re, Pr and Nu from the average cell temperature and pressure.

For both fluids, the mass conservation equation is used to obtain ρ_{i+1}, the momentum conservation one to find p_{i+1} and the energy conservation equation for T_{i+1}.

For the node-centered cells in Fig.3.19, the equilibrium of heat-fluxes was used. Radiation between walls is not considered due to its low expected impact. The wall ends and the exterior face of the outer wall are adiabatic.

Therefore, for the inner wall (iw):

$$\dot{Q}_{cond\_w} - \dot{Q}_{cond\_e} + \dot{Q}_{conv\_n} - \dot{Q}_{conv\_s} = 0 \tag{3.17}$$

Where $\dot{Q}_{cond\_w}$ and $\dot{Q}_{cond\_e}$ represent conduction coming with the western and the eastern node respectively., and where $\dot{Q}_{conv\_n}$ and $\dot{Q}_{conv\_s}$ represent the convection with the northern and the southern fluid cell.

Expanding:

$$-\lambda_w \frac{T_{iw,i} - T_{iw,i-1}}{\Delta x} S_{iw} + \lambda_e \frac{T_{iw,i+1} - T_{iw,i}}{\Delta x} S_{iw} + \alpha_{hp,i'}(\overline{T_{hp,i'}} - T_{iw,i}) S_{iw\_in\_dx} - \alpha_{lp\_iw,i'}(T_{iw,i} - \overline{T_{lp,i'}}) S_{iw\_out\_dx} = 0 \quad (3.18)$$

For the outer wall (ow), and using the same notation as for the inner wall:

$$\dot{Q}_{cond\_w} - \dot{Q}_{cond\_e} + \dot{Q}_{conv\_s} = 0 \quad (3.19)$$

Discretising and expanding:

$$-\lambda_w \frac{T_{ow,i} - T_{ow,i-1}}{\Delta x} S_{ow} + \lambda_e \frac{T_{ow,i+1} - T_{ow,i}}{\Delta x} S_{ow} + \alpha_{lp\_ow,i'}(\overline{T_{lp,i'}} - T_{ow,i}) S_{ow\_in\_dx} = 0 \quad (3.20)$$

For both cases, the conductivities λ_w and λ_e are obtained doing the harmonic average between the current and the adjacent cell as:

$$\lambda_w = \frac{d_{WP}}{\frac{d_{Ww}}{\lambda_W} + \frac{d_{wP}}{\lambda_P}}, \lambda_e = \frac{d_{EP}}{\frac{d_{Ee}}{\lambda_E} + \frac{d_{eP}}{\lambda_P}} \quad (3.21)$$

With the notation being defined as shown in Fig. 3.20, with *d* meaning distance, ***W*** referring to node *i-1*, ***P*** to *i* and ***E*** to *i+1*.

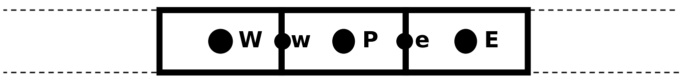

Figure 3.20: Conductivies harmonic average for node-centered discretisation.

Equations (3.13), (3.16), (3.18) and (3.20) form a system of equations with the unknown temperatures of the two flows and the two walls that can be written in the form of A**x** = B, where **x** represents the temperatures at each node. This system is solved for **x** by inverting the matrix A. Another possible way to solve the equations would be by using the Gauss-Seidel Method [1], that is, solving first for one flow, then for the other one, and finally for the walls.

After every step, the temperature map is updated for both methods and compared with the previous map, i.e., checking if convergence is reached. If not, α, C_p, f and λ are re-calculated for the new state and the process is repeated. For that, density and pressure

[1] The Gauss-Seidel Method has been the employed method by the author.

at each node per flow are also needed. The continuity eqs. (3.11) and (3.14) give the former, and momentum conservation eqs. (3.12) and (3.15), give the latter.

Once convergence of all values is reached, the iterative process finishes.

In order to compare this simpler heat exchanger geometry with the mesh-based CFHEX, the same outer dimensions and materials are used. That is, a total length L of 20 cm, an outer wall radius r_o of 2.5 cm, an inner wall thickness t_i of 0.5 mm made of bronze [2], and an outer wall thickness t_o of 0.5 mm made of stainless steel. The inner radius however, has been altered as to maximise the performance of the concentric tube CFHEX[3]. The larger the area of contact with the flows is, the more efficient the heat transfer is going to be. That is why, for the inner pipe, a radius r_i of 2.25 cm has been chosen. Such a configuration leaves a very small area for the LP stream, which creates a higher LP pressure drop. Normally, this is an undesirable feature for the rest of the system. Nevertheless, the following results show that the pressure drop is very small even in the LP pressure. The gain thanks to the increased surface in between the two flows is much more significant than the small increase in pressure drop for the outer flow.

As for the boundary conditions, the warm HP inlet has been set to 290 K while the cold LP inlet to 50 K, simulating the operating conditions of CFHEX1 from Fig. 3.6. Finally, the resultant variation of the pressure drops, the velocity and the density is shown in Fig. 3.21 for a mass flow rate of 100 mg s^{-1}.

Fig. 3.21 confirms the expected behaviour of the velocity and the density. The velocity increases towards the warm end and the density towards the cold end, where the flow contracts. As far as the pressure drop is concerned, it is indeed showing very small values, close to zero for the inner flow and 0.015 mbar for the total pressure drop in the low-pressure pipe. This point may have to be looked into more depth in order to gain confidence in such low values.

Fig. 3.22 shows the temperature profile of both flows and walls. It is interesting to mention that both walls are very close in terms of temperature since they are very close to each other, physically, due to the way the HEX was defined. The coldest point (50 K) is at the outer flow (lp) inlet and the warmest (290 K) is at the inner flow (hp) inlet. The HEX allows reaching the outlet temperature of the high-pressure flow (hp) of 120 K. The overall effectiveness of the configuration is of 71 %. This is roughly 25 % **less** than the same heat exchanger with a mesh in it. Even though the latter presents more pressure drop, the values are still very small and do not affect the system performance significantly. This demonstrates the great potential of meshed based CFHEXs.

[2] Good transversal-axial ratio of heat conduction.

[3] The best possible HEX with the defined outer dimensions and wall materials and thickness is looked for. The inner diameter is the only degree of freedom that can be adjusted to get the best possible performance.

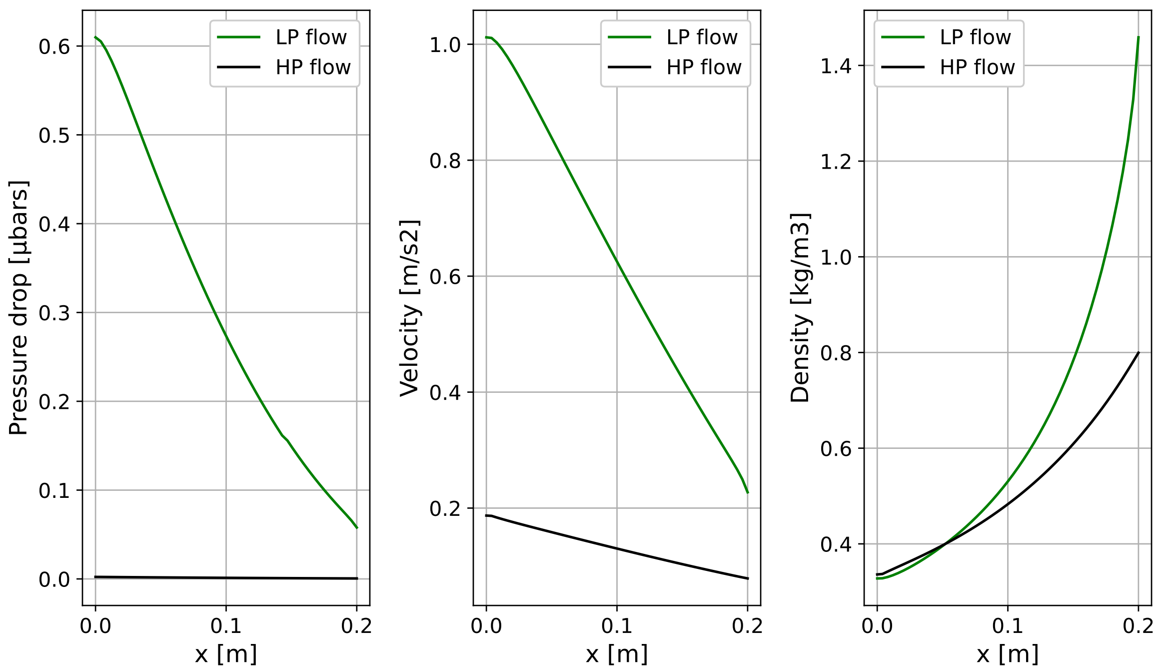

Figure 3.21: Pressure drop, velocity and density (from left to right) profiles along a no-mesh CFHEX. Green lines represent the outer LP flow and black lines, the inner HP flow.

Lastly, a performance analysis of the effectiveness variation with the mass flow rate for the heat-exchanger has been performed. Its results are shown in Fig. 3.23, which shows that the effectiveness decreases with the mass flow rate. This happens as, for such designs, it becomes harder to transfer the heat from from one flow to another due to a significant reduction in the heat transfer area. It is also important to mention that the boundary conditions where set at lower temperatures for this analysis. Concretely at $50\,\mathrm{K}$ for the warm end and at $12\,\mathrm{K}$ for the cold end. It can be noted that for $100\,\mathrm{mg\,s^{-1}}$, the effectiveness has been reduced to $52\,\%$, which is $27\,\%$ lower than for the warmer boundary conditions.

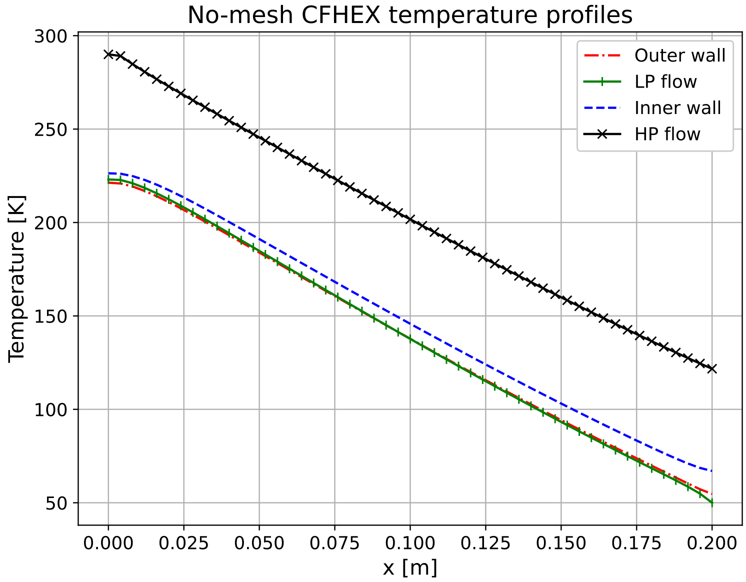

Figure 3.22: Temperature profile along the no-mesh HEX.

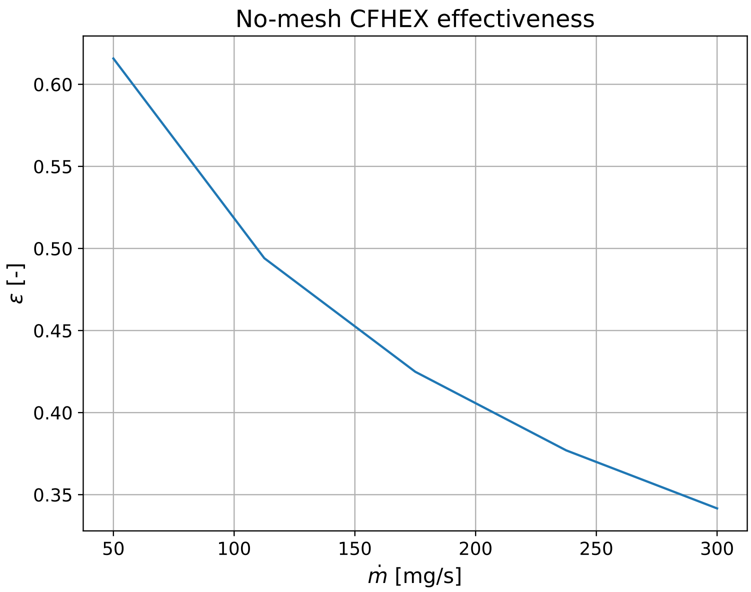

Figure 3.23: Effectiveness variation with mass flow rate for a concentric HEX geometry without mesh.

Chapter 4

Cryogenic properties library

The analysis of different remote cooling systems from Sec. 2.3, the CFHEX measurements data post-processing from Sec. 3.3, and the CFHEX numerical analysis from Sec. 3.4, depend on equations of state for calculating the thermodynamic properties of the fluid, mainly enthalpies for a given pressure and temperature. The ideal gas equation of state (EOS) relates three state variables,

$$p = \rho r T \tag{4.1}$$

where p is the pressure, ρ is the density, r the specific gas constant, and T the temperature. Hence, for a given fluid and two of the state variables, the third can be obtained. As for the enthalpy, it can be determined using ideal gas approximations for the heat capacity, c_p. Nevertheless, the ideal gas EOS is a model of the real gas behaviour, which is only accurate at low pressures and moderate temperatures. Other models need to be used if some level of accuracy is desired outside of this range, and even more so at low temperatures.

The numerical analysis and data post-processing presented in this report were all performed in Python. Python is a general-purpose, high-level programming language, that has become ubiquitous in the last years. It has a very large set of freely available libraries for many different applications. These simplify many tasks, making programming a much faster and simpler process.

CoolProp [7] is one example of a Python library that implements a more precise model of real gas behaviour at an extended range of conditions. It uses an advanced approach with several cubic EOS [10], supporting 122 different components, helium included. Due to its ease of use and implementation, this library has been used successfully and consistently by the Cryolab for temperatures above helium lambda point (see Sec. 1.2.3). However, when temperatures below T_λ were reached for one of the system analysis studies, CoolProp started behaving unexpectedly, returning inconsistent values. Since the helium model used in the analysis is based on unpublished coefficients, it was decided to implement a more robust solution.

HEPAK is a computer FORTRAN routine developed by Horizon Technologies [16], based on the NIST Technical Note 1334 of 1989. It is focused on helium-4[1] properties, and the Cryolab has good experience from using it in the past. Its operating range is well-defined in its specifications, where it is stated that *"The state equations are valid from* 0.8 K *or the melting line to* 1500 K*, including the superfluid range, the lambda line, and liquid vapor mixtures. As a function of pressure, calculations are valid up to* 1000 bar*, except between* 80 K *and* 300 K *where they are valid to* 20 000 bar*"*. The positive previous experience, added to the clearly defined ranges, make HEPAK the preferred solution for the Cryolab. However, its functions are only accesible by directly calling the FORTRAN routine or through an Excel Add-In, which is also provided. At the Cryolab, FORTRAN has come in disuse in the later years and engineers willing to work with it are scarce. While the Excel Add-In is an interesting option, it is not suitable for iterative complex calculations. Python has proved to be a much more advanced and adapted tool, both for analysis and data post-processing.

In this context, it was decided to develop a wrapper code, which would make the HEPAK FORTRAN functions available in Python. That would enable the Python programs that were previously using CoolProp, to transition into HEPAK almost seamlessly.

4.1 HEPAK wrapper for Python

HEPAK is a proprietary program and a license is required to use it, thus no details about its source code can be shown in this report. For the wrapper to work, the FORTRAN source code needs to be compiled as a shared library beforehand. Out of the different existing compilers, *gfortran* with the *-shared* option was used for this purpose.

Once HEPAK is in a shared library state, it can be called with Python's *ctype* internal module, the task of which is interacting with external compiled codes. The focus, from now on, will be purely on the wrapper. An internal Git[2] repository has been established so that anyone within the Cryolab can access, use, and improve the wrapper if desired or needed. Documentation has been added in the repository with the aim of simplifying the familiarisation of the first time user. The existing functions available in the wrapper

[1] Helium-4 refers to its most common stable isotope, which is also the most abundant one in the atmosphere of Earth and the one used by the coling systems described in this document.

[2] Git is a version control system for tracking changes in software development. It enables teams to work together in a very efficient and safe way.

are explained there and examples on how to use them are provided.

The wrapper only accepts Python 3, otherwise it raises an exception. Also, this version is adapted for Windows. If the wrapper were to be used in Linux, the module "WinDLL" would need to be replaced as it is only available in Windows. Even though Python is a dynamically typed language[3], it can be seen in Lis. 4.1 that variables are statically typed. This is needed because HEPAK only accepts pointers, that is, addresses in memory.

```python
"""
Created on Wed Jul 29 13:30:32 2020

@author: bnaydeno
"""

from ctypes import cdll, c_int, c_double, byref, c_long, WinDLL
import os, sys

PYTHON_VERSION = sys.version_info

if PYTHON_VERSION[0] < 3:
    raise Exception("Version 3 of Python is needed")

def getLib():
    if PYTHON_VERSION[1] > 7:
        return WinDLL(os.path.join(
            os.path.dirname(__file__),
            'heprop.dll'), winmode = 0x8
        )
    else:
        return cdll.LoadLibrary(os.path.join(
            os.path.dirname(__file__),
            'heprop.so')
            )

# Returns enthalpy for for a given pressure p, and temperature T.
def h_pT(p, T):

    t = getLib()

    # OUTPUTS

    IDID = c_int()
    PRP = ((c_double * 42) * 3)()
```

[3] For a statically typed language such as FORTRAN, variable types must be manually defined before compiling the code. Python is a dynamically typed language, but since it is being used to wrap FORTRAN, the *ctype* module is being used to define the type of each variable.

```
# INPUTS
JOUT = c_int(11000)
J1 = c_int(1)
VALU1 = c_double(p)
J2 = c_int(2)
VALU2 = c_double(T)
JPRECS =  c_int(2)
JUNITS = c_int(1)

try:
    t.calc_(byref(IDID), byref(PRP), byref(JOUT), byref(J1), \
            byref(VALU1), byref(J2), byref(VALU2), byref(JPRECS), \
            byref(JUNITS))
except:
    print("Unhandled Exception")


if IDID.value < 0:
    raise Exception('The calculation has failed. Check IDID = '\
            + str(IDID.value) +' in HEPAK\'s documentation.')


return PRP[0][9]
```

Listing 4.1: Snippet of the wrapper showing the main function *getLib()*, that calls the shared library, and one example function *h_pT(p, T)*, that shows how the enthalpy would be calculated when provided with the temperature and the pressure.

Several useful functions were integrated in the full version of the wrapper, so that the user can quickly start extracting useful data. These are the following, where pressure is always given in Pa, the temperature in K and the specific enthalpy in J/kg:

- **h_pT(p,T)** : Computes the specific enthalpy in J/kg, given the pressure and the temperature.
- **T_ph(p,h)** : Computes the temperature in K, given the pressure and the specific enthalpy.
- **h_p_sL(p)** : Returns liquid phase specific enthalpy in J/kg for saturated conditions at pressure "p".
- **h_p_sV(p)** : Returns vapour phase specific enthalpy in J/kg for saturated conditions at pressure "p".
- **getPRP(...)** : Generic function that computes any of the available HEPAK parameters. Its details are confidential.
- **HeCalc(...)** : Generic function that mimics the way HEPAK's Excel Add-In works,

which is very familiar interface in the Cryolab. Its details are also confidential.

Building a wrapper for Python actually made it very easy to also implement it into Matlab, as the recent versions of the latter come with an integrated Python interface. Since Matlab is largely used in the laboratory, an example describing how to call the wrapper and consequently, HEPAK, directly from Matlab, has been added to the Git repository. Having Python installed on the computer is the only requirement to use it.

Finally, during the development and testing process, it was discovered how the shared HEPAK library can be used directly from a C program. Hence, an example of how to do that was also added to the repository with the idea to help users that may need it. What started as a project to enable Python programs to call HEPAK's FORTRAN program, eventually covered C and Matlab as well (see Fig. 4.1).

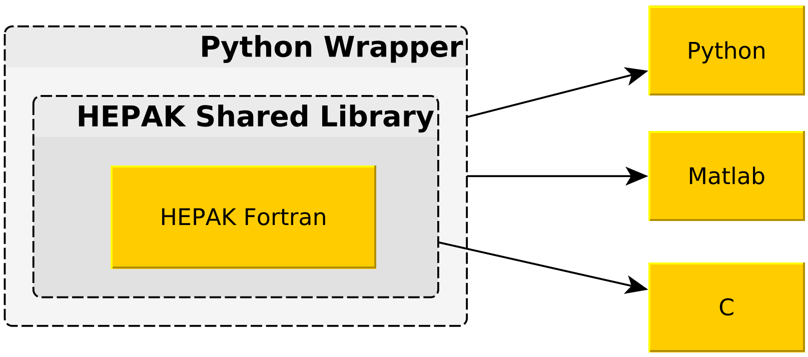

Figure 4.1: High-level view of HEPAK wrapper and its interfaces, namely Python, Matlab and C. While Python and Matlab would use the Python Wrapper, C would use the compiled shared library directly.

4.2 Integration into existing programs

Listings 4.2 and 4.3 show how the wrapper would be used from a Python and a Matlab code respectively. There are more complex functions like *getPRP(...)* and *HeCalc(...)* which have more functionality. This integration has not been included here, but it is available in the internal Git repository.

```
import sys
sys.path.insert(0, 'hepak-py-wrap-path')

import hepak_wrapper as hp

h = hp.h_pT(100000,300)
```

Listing 4.2: Example on how to call *h_pT* from another Python code. 'hepak-py-wrap-path' represents the location of the wrapper from Lis. 4.1.

```
hp = py.importlib.import_module('hepak-py-wrap-path');

h = hp.h_pT(100000,300);
```

Listing 4.3: Example on how to call *h_pT* from Matlab. 'hepak-py-wrap-path' represents the location of the wrapper from Lis. 4.1.

An important last consideration needs to be made when transitioning from CoolProp to the HEPAK's wrapper. The absolute value of enthalpy at a certain point is not an easy value to determine, however, for many analysis it is rather the enthalpy change during a process in question that is more important. Therefore, the example function *h_pT* returns a relative enthalpy to a reference point. When two enthalpies are subtracted from each other, the reference point is cancelled out and only the change of enthalpy remains, giving valuable information about the process in-between. But, if the reference point of the two enthalpies is different, it is not going to cancel out when the two enthalpies are substracted, inducing erroneous results. This can happen if CoolProp and HEPAK are used together, as both use different reference points[4]. Because of that, using only HEPAK has been recommended to avoid such errors.

[4]Several tests were performed to determine if the reference point was the same.

Conclusion and perspectives

Three remote cooling systems, depicted in Fig. 2.4, were analysed, and their fitness for different applications has been assessed. The results showed that a high-pressure convection loop (System 1 from Fig. 2.4a), taking helium directly from the cryocooler supply line at 25 bar, is capable of providing up to 0.5 W at 5 K at the cooling interface, with an expected reduced level of vibrations, and in a single-phase flow. A lower pressure system (System 3 from Fig. 2.4c) using an independent pump to circulate helium at 5 bar at its inlet, and a JT-valve expansion upstream of the CIF, reaches 3.5 W at 4.5 K with a two-phase flow at constant temperature. While such configuration is more prone to vibrations, it increases the available cooling power at the cryocooler second stage by more than 75 %. Because of that, it has been deemed that the System 1 is more appropriate for vibration-sensitive applications, where the cooling power is not that critical, and that System 3 is better for the other cases, where achieving a high cooling power is more important. As far as System 2 is concerned (Fig. 2.4b), it has proved to be limited both at low cooling powers and at high mass flow rates. Because of this, the other options were more preferred. Lastly, it was found that a 35 % increase in the system cooling power is achieved for an increase of 5 % in the effectiveness of the CFHEXs, showing the relevance of reaching high effectivenesses values and justifying the research currently being performed at the Cryolab.

A thorough knowledge of cryogenic measurement techniques, materials, sensors, and laboratory equipment has been gained throughout the internship. For the characterisation of the CFHEX design, a cryocooler, a vacuum pump, a circulation pump, and a purging pump had to be operated safely. The laboratory set-up had to be adjusted periodically for the different measurement goals, changing mass flow rates, pressure levels, and temperature conditions. A proper initial training enabled the author to perform the measurements safely, testing the novel heat exchanger designs for its relevant parameters. In turn, the obtained results were post-processed and analysed successfully. Very promising effectiveness values of 98 % have been obtained for the Cryolab's latest CFHEX design, which exceeds the initial expectations. Moreover, very low pressure drops were found along the CFHEX, under 6 mbar for both CFHEX streams. Such low levels allow for a JT-expansion with a higher pressure difference, which in turn increases the cooling power of the system further.

As far as the analytical work on the heat exchanger characterisation is concerned, a concentric tube-in-tube CFHEX design was numerically modelled and its performance was evaluated, with the purpose of comparing it with the more sophisticated options currently analysed at the Cryolab. The results have shown that the enhanced mesh-based CFHEX design allows a significant improvement in the effectiveness by $\sim 25\,\%$ (from $71\,\%$ to $98\,\%$) while maintaining similar dimensions. A thermophysical properties calculation tool, based on HEPAK, was successfully developed to support the numerical model, as well as the system analysis and the data post-processing.

In terms of the future perspectives, the measurements on the novel CFHEX will continue for a different range of operating temperatures in order to fully characterise its performance. The next generation CFHEX will be designed and manufactured with the gained knowledge, consolidating and, potentially, improving the performance. Finally, the range of remote cooling system applications is expanding greatly due their high potential. Once the cooling needs and the relevant heat loads for these applications are defined, the simulation analysis will have to be refined further so that more precise and adapted values can be extracted. More exotic architectures may also be included in the future analysis of alternatives. Adding an ejector in the convective loop is an example of an enhancement that will be considered in the near future.

To finish, the combination of a hands-on experience in the laboratory, measuring, mounting, and debugging, together with a more analytical part, where system simulations had to be performed, gave the project a very good span into the cryogenic technology, its applications, the current state, and the future potential of remote cooling systems. Even though the length of the project has been shortened from six to four months due to external reasons, the set objectives for this time period were accomplished satisfactorily. All in all, it can be concluded that the project has been a very enriching experience.

Bibliography

[1] G. Walker. *Cryocoolers: Part 1: Fundamentals*. International Cryogenics Monograph Series. Springer US, 1983, pp. 83–85. ISBN: 9780306407154. URL: https://books.google.ch/books?id=CcJTAAAAMAAJ.

[2] W.M. Kays and A.L. London. *Compact Heat Exchangers*. Krieger Pub. Co., 1984. ISBN: 9781575240602. URL: http://books.google.de/books?id=A08qAQAAMAAJ.

[3] D.G. Gilmore and M. Donabedian. *Satellite Thermal Control Handbook - Chapter 5: Insulation*. Progress in Astronautics and Aeronautics Series. Aerospace Corporation Press, 1994. Chap. 5. ISBN: 9781884989001. URL: https://books.google.ch/books?id=TwiPAAAACAAJ.

[4] A. Green. *The Integration of Liquid Cryogen Cooling and Cryocoolers with Superconducting Electronic Systems*. English. Tech. rep. LBNL-53068-Conf. Ernest Orlando Lawrence Berkeley NationalLaboratory, Berkeley, CA (US), July 2003. URL: https://www.osti.gov/biblio/917813 (visited on 10/01/2020).

[5] I. Efthymiopoulos et al. “HiRadMat: a New Irradiation Facility For Material Testing at CERN”. In: *Proceedings of IPAC2011* (2011).

[6] K.D. Timmerhaus and T.M. Flynn. *Cryogenic Process Engineering*. International Cryogenics Monograph Series. Springer US, 2013. ISBN: 9781468487565. URL: https://books.google.fr/books?id=RfzlBwAAQBAJ.

[7] I. Bell et al. “Pure and Pseudo-pure Fluid Thermophysical Property Evaluation and the Open-Source Thermophysical Property Library CoolProp”. In: *Industrial & Engineering Chemistry Research* 53.6 (2014), pp. 2498–2508. DOI: 10.1021/ie4033999. eprint: http://pubs.acs.org/doi/pdf/10.1021/ie4033999. URL: http://pubs.acs.org/doi/abs/10.1021/ie4033999.

[8] CTTC-UPC-ETSEIAT. *Formulae for the resolution of fluid dynamics and heat and mass transfer problems*. v5a. 2015.

[9] L. Duband. “Space Cryocooler Developments”. In: *Physics Procedia* 67 (2015), pp. 1–10. DOI: 10.1016/j.phpro.2015.06.003. URL: https://core.ac.uk/download/pdf/82220271.pdf (visited on 10/02/2020).

[10] I. Bell and A. Jäger. "Helmholtz Energy Transformations of Common Cubic Equations of State for Use with Pure Fluids and Mixtures". In: *Journal of Research of the National Institute of Standards and Technology* 121 (June 2016), p. 238. DOI: 10.6028/jres.121.011.

[11] L. Decker. "Overview on Cryogenic Refrigeration Cycles for Large Scale HTS Applications". In: Mar. 2016.

[12] M. Fernandes et al. "Operation of a Cryogenic Current Comparator with Nanoampere Resolution for Continuous Beam Intensity Measurements in the Antiproton Decelerator at CERN". In: *9th International Particle Accelerator Conference IPAC2018* (2018). DOI: 10.18429/JACoW-IPAC2018-THPML044.

[13] *About | CERN*. URL: https://home.cern/about/ (visited on 10/15/2020).

[14] Cryogenic Society of America, Inc 218 Lake Street Oak Park, and Illinois 60302-2609 USA Phone: 1-708-383-6220 Fax: 1-708-383-9337. *Cryo Central*. en-US. URL: https://cryogenicsociety.org/resources/cryo_central/ (visited on 10/15/2020).

[15] Bronkhorst. *F-113AI*. URL: https://www.bronkhorst.com/int/products/gas-flow/in-flow/f-113ai/ (visited on 10/11/2020).

[16] *Horizon Technologies HEPAK Software*. URL: http://www.htess.com/hepak.htm (visited on 10/18/2020).

[17] *Products - SHI Cryogenics Group*. en. URL: http://www.shicryogenics.com/products/ (visited on 10/15/2020).

[18] *PT420*. en-US. URL: https://www.cryomech.com/products/pt420/ (visited on 10/17/2020).

[19] *ZEROe*. en. URL: https://www.airbus.com/innovation/zero-emission/hydrogen/zeroe.html (visited on 10/15/2020).

Abstract — A remote cooling system is a promising technology that could close the existing gap in cooling power between the powerful cryoplants and the compact, low-power, cryocoolers. Such a system could be accomplished by adding a carefully designed convection loop to a cryocooler. Such an upgrade has several advantages, notably decoupling mechanically and by distance the cooling interface from the cryocooler, enabling applications that could otherwise be harmful for the latter or that are sensitive to vibrations, and increasing the cryocoolers cooling power capabilities. A critical component of the remote cooling systems under development is a counter-flow heat exchanger (CFHEX). Very high CFHEX effectiveness values (above $95\,\%$) are required to achieve high system cooling powers. With that in mind, the focus of this project is twofold. On the one hand, an analysis of different remote cooling system architectures was performed to determine their best fitness for a range of applications. The prototype systems were found to reach $\sim 3.5\,\mathrm{W}$ of cooling power with only $2\,\mathrm{W}$ available at the cryocooler alone, both at $4.5\,\mathrm{K}$. On the other hand, several measurement campaigns and its data post-processing were carried out on a novel CFHEX design. Effectiveness values of up to $98\,\%$ were reached, exceeding the initial $95\,\%$ goal.

Keywords : Cryogenics, cryocooler, helium, remote cooling system, heat exchanger, effectiveness, CERN.

ISAE-SUPAERO
31055 Toulouse
France

UPC
08034 Barcelona
Spain

CERN
1211 Geneva
Switzerland